FISEVIER

Contents lists available at ScienceDirect

Journal of Volcanology and Geothermal Research

journal homepage: www.journals.elsevier.com/journal-of-volcanology-and-geothermal-research





Outgassing through magmatic fractures enables effusive eruption of silicic magma

Josh Crozier^{a,*}, Samantha Tramontano^b, Pablo Forte^c, Sarah Jaye C. Oliva^d, Helge M. Gonnermann^e, Einat Lev^f, Michael Manga^g, Madison Myers^h, Erika Raderⁱ, Philipp Ruprecht^j, Hugh Tuffen^k, Rebecca Paisley^l, Bruce F. Houghton^m, Thomas Shea^m, C. Ian Schipperⁿ, Jonathan M. Castro^o

- ^a U.S. Geological Survey California Volcano Observatory, 350 N Akron Road, Moffett Field, CA 94035, USA
- ^b City University of New York, The Graduate Center, 365 Fifth Avenue, New York, NY 10016, USA
- c Instituto de Estudios Andinos (IDEAN) (UBA CONICET), Intendente Güiraldes 2160 Ciudad Universitaria, Buenos Aires, Argentina
- ^d University of Victoria, School of Earth and Ocean Sciences, 3800 Finnerty Road, Victoria, BC V8P 5C2, Canada
- ^e Rice University Earth, Environmental, and Planetary Sciences, MS-126 6100 Main Street, Houston, TX 77005, USA
- f Columbia Lamont-Doherty Earth Observatory, 61 Route 9W, Palisades, NY 10964-1000, USA
- g University of California at Berkeley Earth and Planetary Science, 307 McCone Hall, Berkeley, CA 94720-4767, USA
- ^h Montana State University Earth Sciences, P.O. Box 173480, Bozeman, MT 59717-3480, USA
- ⁱ University of Idaho Geography and Geological Sciences, 875 Perimeter Drive MS 3021, Moscow, ID 83843-3021, USA
- ^j University of Nevada at Reno Geological Sciences and Engineering, 1664 N. Virginia Street, Reno, NV 89557-0172, USA
- k Lancaster University Environment Centre, Lancaster LA1 4YQ, United Kingdom
- ¹ Cornish Lithium Ltd, Tremough Innovation Centre, Penryn, Cornwall TR10 9TA, United Kingdom
- m University of Hawaii at Manoa Earth Sciences, 1680 East-West Road, Honolulu, HI 96822, USA
- ⁿ Victoria University of Wellington, Geography, Environment, and Earth, PO Box 600, Wellington 6023, New Zealand
- ^o Johannes Gutenberg Universität Mainz Institute of Geosciences, J.-J.-Becher-Weg 21, D-55128 Mainz, Germany

ARTICLE INFO

Keywords: Cordón Caulle volcano Silicic Hybrid eruption Tuffisite Outgassing Explosive-effusive Conduit model

ABSTRACT

Several mechanisms have been proposed to allow highly viscous silicic magma to outgas efficiently enough to erupt effusively. There is increasing evidence that challenges the classic foam-collapse model in which gas escapes through permeable bubble networks, and instead suggests that magmatic fracturing and/or accompanying localized fragmentation and welding within the conduit play an important role in outgassing. The 2011–2012 eruption at Cordón Caulle volcano, Chile, provides direct observations of the role of magmatic fractures. This eruption exhibited a months-long hybrid phase, in which rhyolitic lava extrusion was accompanied by vigorous gas-and-tephra venting through fractures in the lava dome surface. Some of these fractures were preserved as tuffisites (tephra-filled veins) in erupted lava and bombs. We integrate constraints from petrologic analyses of erupted products and video analyses of gas-and-tephra venting to construct a model for magma ascent in a conduit. The one-dimensional, two-phase, steady-state model considers outgassing through deforming permeable bubble networks, magmatic fractures, and adjacent wall rock. Simulations for a range of plausible magma ascent conditions indicate that the eruption of low-porosity lava observed at Cordón Caulle volcano occurs because of significant gas flux through fracture networks in the upper conduit. This modeling emphasizes the important role that outgassing through magmatic fractures plays in sustaining effusive or hybrid eruptions of silicic magma and in facilitating explosive-effusive transitions.

^{*} Corresponding author at: 350 N Akron Road, Moffett Field, CA 94035, USA.

E-mail addresses: jcrozier@usgs.gov (J. Crozier), stramontano@gradcenter.cuny.edu (S. Tramontano), fortep@gl.fcen.uba.ar (P. Forte), soliva@uvic.ca (S.J.C. Oliva), helge@rice.edu (H.M. Gonnermann), el2545@columbia.edu (E. Lev), manga@seismo.berkeley.edu (M. Manga), madison.myers@montana.edu (M. Myers), erader@uidaho.edu (E. Rader), pruprecht@unr.edu (P. Ruprecht), h.tuffen@lancaster.ac.uk (H. Tuffen), bhought@soest.hawaii.edu (B.F. Houghton), tshea@hawaii.edu (T. Shea), ian.schipper@vuw.ac.nz (C.I. Schipper), castroj@uni-mainz.de (J.M. Castro).

1. Introduction

Silicic volcanic eruptions involving highly viscous dacitic to rhyolitic magmas exhibit a wide range of explosivity and mass discharge rates, both between different eruptions and during a single eruption (Cassidy et al., 2018). These eruptions cause a variety of threats to humans, infrastructure, and the environment (Major and Lara, 2013; Elissondo et al., 2016). Understanding the conditions under which different types of eruptive activity occur is thus important in assessing potential eruptive hazards as well as how these hazards might evolve during an eruption (National Academies of Sciences, 2017).

As magma ascends, decompression drives the exsolution of magmatic volatiles into a fluid phase and leads to the expansion and coalescence of bubbles (Gonnermann and Manga, 2007) (Fig. 1). In most cases, magma is sufficiently volatile-rich that decompression to atmospheric pressure without outgassing would yield porosities approaching 100% (Wallace et al., 2015). However, as magma rises, increasing volume and buoyancy lead to increased magma ascent velocities and decompression rates, which can eventually cause sufficiently high strain rates to induce conduit-spanning brittle fragmentation, particularly in more viscous silicic magmas (Papale, 1999). For an effusive eruption to occur, some amount of outgassing, i.e., decoupling of the gas phase from the melt, will generally need to occur during magma ascent (Eichelberger et al., 1986). In high viscosity silicic magma, the rates of magma ascent are typically faster than the rates at which bubbles buoyantly rise through melt, so outgassing must occur via permeable flow of gas either upward through the magma column or outward through the adjacent wall rock (Woods and Koyaguchi, 1994; Okumura et al., 2008) (Fig. 1). In contrast, mafic magmas typically have viscosities many orders of magnitude lower than silicic magmas, which results in significantly different ascent dynamics (Gonnermann et al., 2013). Outgassing in mafic magma can be more readily facilitated by buoyant bubble rise

Table 1
Conduit magma ascent model parameters.

Parameter	Default value	Description
g	9.8 m/s^2	Gravitational acceleration
c_s	4.11×10^{-6}	Gas (H ₂ O) saturation constant
μ_g	1×10^{-5} Pas	Gas (H ₂ O) viscosity
R_g	462 J/(kgK)	Specific gas constant for H ₂ O
T	1173 K	Magma temperature
$C_{initial}$	4 wt%	Initial (total) volatile (H2O) content
$q_{initial}$	$1 \times 10^4 \text{kg/s}$	Initial total (volatiles + melt) vertical mass flux
P_{base}	82 MPa	Pressure at base of conduit
P_{atm}	0.1 MPa	Atmospheric (vent) pressure
ρ_m	2400 kg/m ³	Melt density
b	$10^{-8.892}$	Bubble network permeability constant
n	2	Bubble network permeability constant
$n_{compact}$	2.8	Bubble network permeability constant
ϕ_{crit}	0.7436	Bubble network percolation threshold
c_k	1.353 1/m	Bubble network inertial permeability
		constant
d_k	8.175 m	Bubble network inertial permeability
		constant
N_f	10	Number of fractures
c_{\in}	0.25	Fracture wall roughness height scale
		constant
r_{base}	[solved to fit boundary conditions]	Base conduit radius
L	3000 m	Conduit length
r_{flare}	30 m	Vent flare radius
z_{flare}	-250 m	Vent flare depth
ϕ_{max}	85%	Maximum porosity threshold
ϕ_{vent}	25%	Final (vent) porosity threshold
$z_{compact}$	-250 m	Compaction threshold depth
k_w	10^{-14} m^2	Wall rock permeability
L_w	100 m	Wall rock pressure diffusion length
	. 2	scale
ρ_w	2800 kg/m ³	Wall rock density

through the melt, and if fragmentation occurs it usually involves fluid-dynamical breakup rather than brittle processes (Gonnermann, 2015). We thus only address silicic volcanism here.

Permeable bubble networks will naturally develop when porosity exceeds the percolation threshold (around 75% without shear or as low as 30% during shear), and hysteresis-dependent bubble-network permeability during magma compaction (or foam-collapse) allows permeability to remain elevated as porosity decreases (Okumura et al., 2008, 2009; Gonnermann et al., 2017). Shear localization may focus permeable gas escape pathways near conduit walls and either help or hinder overall outgassing depending on ascent rate (Okumura et al., 2009, 2013).

1.1. Magmatic fractures

There is increasing recognition that extrusion of outgassed silicic lava can also involve gas escape facilitated by brittle failure of magma through magmatic fragmentation and/or fracturing, which has been inferred from seismicity (Tuffen et al., 2008), petrology (Unwin et al., 2021), and visual observations of the recent rhyolitic eruptions of Chaitén (2008-2011) and Cordón Caulle (2011-2012) volcanoes, both in Chile (Castro et al., 2012; Schipper et al., 2013). Here we will use the term fragmentation to refer to disaggregation of magma into discrete particles, and the term magmatic fracturing to refer to opening of cracks in the magma column, though the processes associated with both can be similar. Fragmentation does not necessarily lead to a fully explosive eruption since it can be followed by welding (Gonnermann and Manga, 2003; Tuffen et al., 2003; Vasseur et al., 2013; Kendrick et al., 2016; Saubin et al., 2016; Kolzenburg et al., 2019; Lamur et al., 2019; Wadsworth et al., 2020). Here we use the term welding (also referred to as sintering in some publications) to refer to the adhesion and eventual fusion that occurs when the surface of a hot magma particle or the surface of a magmatic fracture contacts other magmatic surfaces or conduit wall rock (Vasseur et al., 2013; Gardner et al., 2018). Fragmentation can also be localized, e.g., constrained within magmatic fractures (Castro et al., 2014; Black et al., 2016; Kendrick et al., 2016; Saubin et al., 2016) (Fig. 1). Magmatic fractures can form due to localized fragmentation, shear stress at the conduit margins, or tensile stress caused by flow divergence (e.g., from a widening conduit, expanding lava dome/flow, or accelerating magma ascent) (Gonnermann and Manga, 2003; Tuffen et al., 2003; Neuberg et al., 2006; Okumura et al., 2010; Heap et al., 2015).

Chaitén and Cordón Caulle volcanoes have provided unprecedented context for how fractures relate to eruption dynamics (Castro et al., 2014; Saubin et al., 2016; Paisley et al., 2019a, 2019b; Schipper et al., 2021). Both eruptions involved initial fully explosive (Plinian to sub-Plinian) phases (Castro et al., 2013; Schipper et al., 2013; Tuffen et al., 2013). The explosive phases then transitioned to hybrid (or simultaneous) explosive-effusive activity, during which time extrusion of low-porosity lava was accompanied by weaker gas and tephra venting from fractures in the lava dome/flow surface (Figs. 1, 2). At Chaiten this was followed by a final fully effusive phase, in which lava emission occurred without any visible tephra venting.

Fractures can be preserved as tuffisites, which are tephra-filled veins found within and around dissected or intercepted volcanic conduits. Henceforth we will use the term tuffisite to refer to 'internal' tuffisites that form within magma rather than 'external' tuffisite veins emplaced into adjacent wall rock (Unwin et al., 2021). Tuffisites are now recognized and documented in many eruptions including Cordón Caulle volcano (Schipper et al., 2021) (Fig. 1), Chaitén (Saubin et al., 2016), Mono Lake, USA (Black et al., 2016), Colima, Mexico (Kendrick et al., 2016), Mule Creek, USA (Stasiuk et al., 1996); Torfajökull, Iceland (Tuffen and Dingwell, 2005; Berlo et al., 2013); and Unzen, Japan (Noguchi et al., 2008). These systems exhibiting magmatic fractures encompass a wide range of eruptive conditions: total eruption volumes from 0.002 to >20 km³, eruption rates from <0.1 to >70 m³/s,

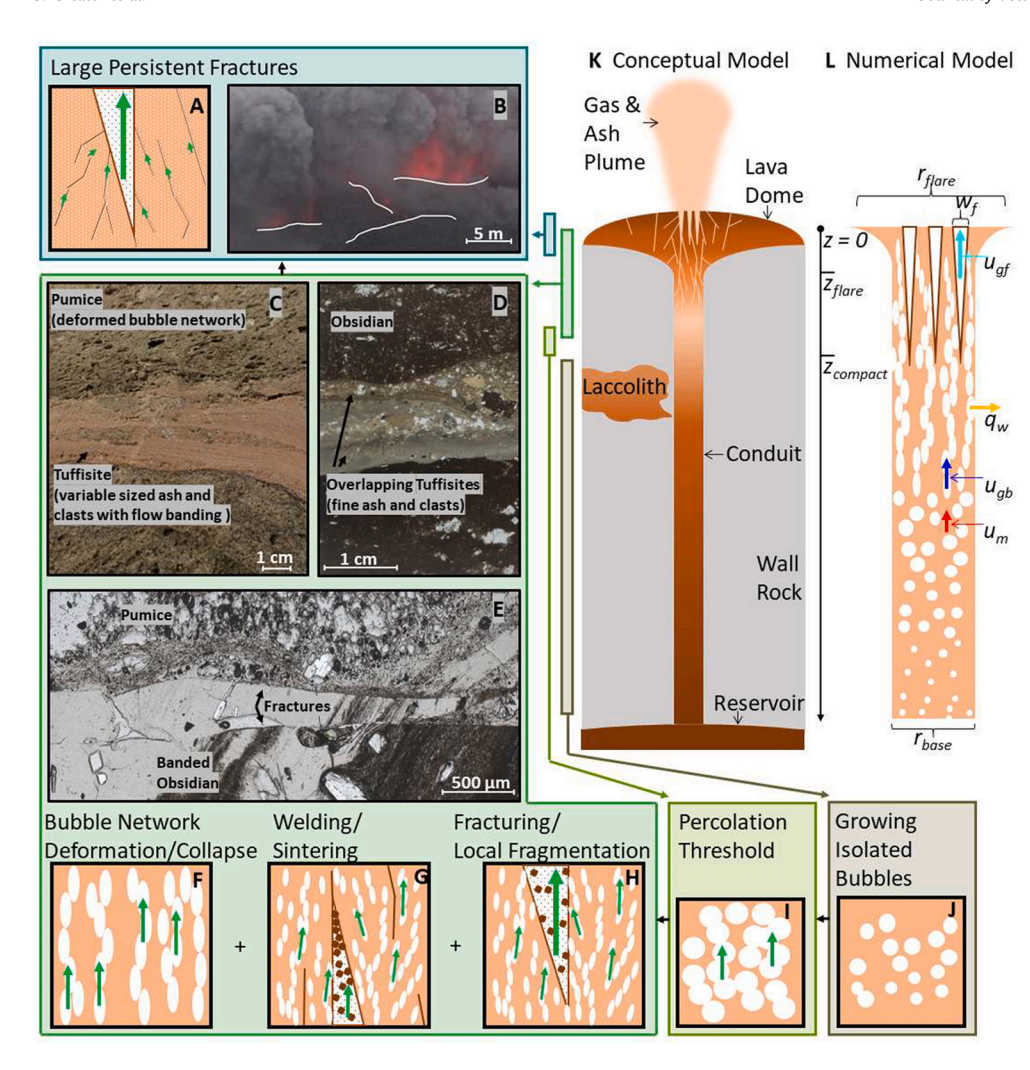


Fig. 1. Conceptual model of the hybrid phase of the Cordón Caulle volcano eruption. A. Sketch of proposed near-vent fracture network geometry. B. Video frame outlining locations of visible lava dome surface venting at Cordón Caulle volcano on January 10, 2012. C. Photo showing a tuffisite vein cutting through pumice. D. Thin section of two overlapping tuffisite veins cutting through obsidian. E. Thin section of fractures cutting through banded obsidian and pumice. F. Sketch of bubble network deformation/ collapse. G. Sketch of fracture welding and tephra sintering within fractures. H. Sketch of fracturing and localized fragmentation within fractures. I. Sketch of bubble network percolation onset. J. Sketch of growing isolated bubbles at depth. K. Conduit-scale conceptual model sketch. L. Numerical model sketch.

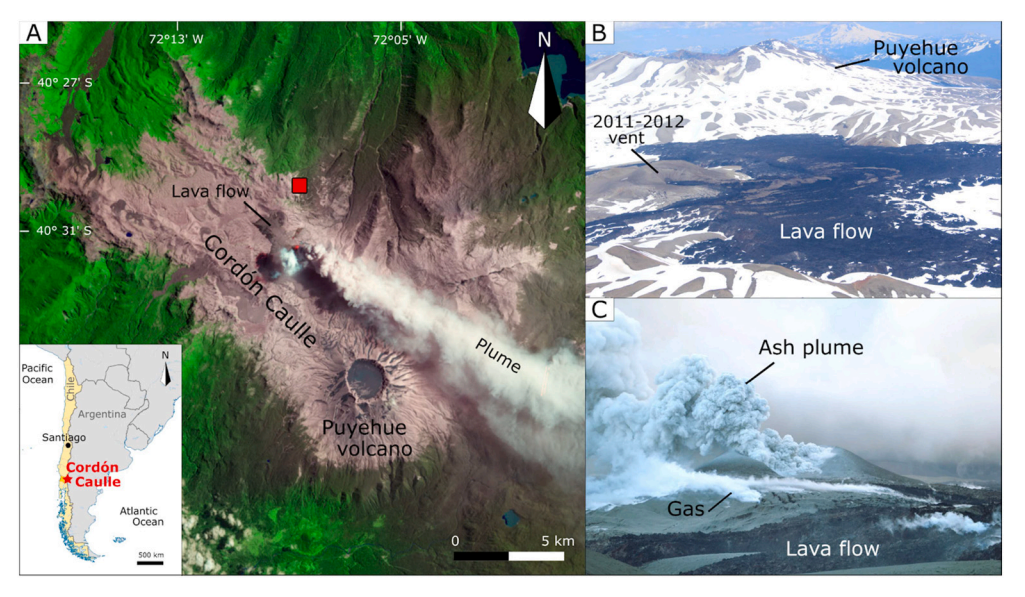


Fig. 2. Location and main features of the Puyehue Cordón Caulle volcanic complex, including the 2236 m a.s.l. Puyehue volcano stratocone and the Cordón Caulle volcano fissure system (~1500 to 1793 m a.s.l) that sourced the 2011-2012 eruption. A. Falsecolour satellite image from NASA's Earth Observing-1 (EO-1) Advanced Land Imager during the hybrid eruption phase on January 26, 2012 (Allen and Simmon, 2012). Red square indicates the observation point from which videos used in this work were taken. B. Post-eruption photo from a light aircraft on December 5, 2017. C. Photo from January 12, 2012, of the hybrid eruptive phase. (For interpretation of the references to colour in this figure legend, the reader is referred to the web version of this article.)

phenocryst content from 1 to 50 vol%, and initial magmatic H_2O content from 2 to 7 wt%. Fracturing may be ubiquitous in silicic systems, just not yet searched for or not well preserved in the full eruption record. Geochemical evidence such as trace element heterogeneities, as well as

textural evidence such as vesicle morphologies and remnant clasts, both suggest that at least some silicic lava consists entirely of fractured and/or fragmented material that has undergone varying degrees of welding and subsequent deformation (Tuffen et al., 2003; Gonnermann and

Manga, 2003; Castro et al., 2012, 2014; Paisley et al., 2019a; Wadsworth et al., 2020).

1.2. Open questions

While conduit-scale models have shown that stress states during magma ascent could induce magmatic fracture formation (Gonnermann and Manga, 2003), no conduit-scale models have explicitly accounted for gas flow through fractures. Models of gas transport from melt to magmatic fractures via chemical diffusion have shown that very close fracture spacing (on the order of 0.01-1 mm) would be required for fractures to facilitate a rate of magma outgassing consistent with observed rates of outgassed lava extrusion (Castro et al., 2012; Pallister et al., 2013). However, if fractures intercept permeable magma then gas transport rates to fractures could be greatly increased (Castro et al., 2014). Additionally, although many conduit-scale models have considered permeable gas escape through bubble networks and wall rock (Woods and Koyaguchi, 1994; Jaupart, 1998; Slezin, 2003; Melnik et al., 2005; Kozono and Koyaguchi, 2009a, 2012; Degruyter et al., 2012; La Spina et al., 2017; Manga et al., 2018), hysteresis-dependent bubble network permeability during magma compaction has only been considered in limited scenarios (Michaut et al., 2009; Wong et al., 2017).

There are thus still key limitations in both our conceptual and quantitative understanding of fracture-mediated outgassing in hybrid/effusive silicic eruptions. Three important questions are: (1) Can outgassing, solely via permeable bubble networks in magma and/or via adjacent permeable wall rock, permit eruption of low-porosity lava? (2) If not, could enhanced outgassing via magmatic fracture networks facilitate eruption of low-porosity lava, without requiring full conduit-spanning brittle fragmentation? (3) How do factors such as magma discharge rate and conduit geometry affect the answers to these questions?

We address these questions by combining models of magma ascent in volcanic conduits with available constraints on eruption parameters. We focus primarily on the 2011-2012 Cordón Caulle volcano eruption, where video of surface fracture venting provides additional constraints. We compile existing observations of this eruption with new video analyses of gas and tephra venting and use these to inform a 1D (onedimensional), two-phase steady-state model of magma ascent that accounts for gas escape through permeable bubble networks, magmatic fractures, and wall rock (Fig. 1). This model allows us to examine whether outgassing through magmatic fractures is required to facilitate the observed eruption of low-porosity lava at Cordón Caulle volcano, quantify the amount of outgassing that these fractures would need to accommodate, and obtain some bounds on fracture onset depth and fracture widths. We then extrapolate the results of this case study to address the importance of magmatic fractures in outgassing and eruptive dynamics more generally.

2. Background on the 2011–2012 Cordón Caulle volcano eruption

The 2011–2012 Cordón Caulle volcano eruption in the Southern Volcanic Zone, Chile, is among the largest eruptions of the 21st century to date, emitting about 1 km³ of rhyolite tephra (Pistolesi et al., 2015), emplacing a 0.8 km³ laccolith and a 0.6 km³ lava flow (Castro et al., 2016; Delgado et al., 2019; Delgado, 2021) (Fig. 2), and causing a wide range of economic, health, and environmental impacts (Wilson et al., 2013; Elissondo et al., 2016; Forte et al., 2018). Magma was stored 2.5 to 10 km deep at temperatures of 870 to 920 °C (Castro et al., 2013; Jay et al., 2014; Seropian et al., 2021). Pyroxene-hosted melt inclusions in the pyroclasts record pre-eruptive (storage) volatile contents up to 3.9 (\pm 0.7) wt% H₂O and 220 ppm CO₂ (Jay et al., 2014). Residual bulk and groundmass glass H₂O contents reported for 2011–2012 erupted products were uniformly low (< 0.35 wt%) and almost completely outgassed to atmospheric pressure for all eruptive phases (Schipper et al., 2013;

Castro et al., 2014). Rare mafic enclaves found in erupted products suggest that the erupted crystal-poor rhyolite was fed from a basaltic mush with minor direct mafic recharge. These basaltic magmas brought in a deeper supply of melt, volatiles, and heat, which likely influenced the generation of an eruptible magma body in the mid-upper crust (Winslow et al., 2022).

After two months of precursory seismic activity, the eruption began on June 4, 2011, with a fully explosive (sub-Plinian, VEI ~4-5) phase (Castro et al., 2013). The climactic part of this phase lasted one day and produced eruptive columns reaching up to 14 km above the vent and mass flow rates of $\sim 10^7$ kg/s (Bonadonna et al., 2015). The explosive phase continued for ten days at decreasing intensity. Emplacement of a ~ 200 m deep laccolith occurred primarily between June 8 and July 3 at a magma flux of up to 150 m 3 /s (\sim 10 6 kg/s) (Castro et al., 2016; Delgado, 2021). The hybrid eruptive phase was marked by the onset of extrusion of mostly outgassed rhyolite lava on June 15th, with an extrusion rate of 40 m³/s (Bertin et al., 2015). The maximum extrusion rate of 70 m³/s occurred 8 days later on June 23. Extrusion continued for nine months at an average rate of 17 m³/s, the time period we primarily focus on due to available video from January 2012 (Schipper et al., 2013). Lava extrusion was accompanied by passive outgassing of the lava flow (Tuffen et al., 2013) and persistent vigorous gas and tephra venting of varying intensity (Figs. 1, 2), with characteristics typically associated with weak explosive activity such as semi-continuous tephra jetting, ejection of ballistic material, and Vulcanian-like blasts (Schipper et al., 2013). During this period eruptive columns were < 6 km high (SERNAGEOMIN-OVDAS, 2010-2012) with a mass rate of ejection << 10⁶ kg/s (Bonadonna et al., 2015). Extruded lava continued to flow at least until January 2013 despite magma supply ceasing in late March 2012 (Tuffen et al., 2013).

The 2011-2012 Cordón Caulle volcano eruption emitted a wide spectrum of pyroclastic material -from very fine ash to meter-size bombs— as well as lava (Figs. 1, 2). Neither bulk rock SiO2 concentration (69.5 to 71 wt%) nor phenocryst content (< 5%) showed significant variations among the different eruptive products and phases (Castro et al., 2013; Jay et al., 2014; Alloway et al., 2015; Schipper et al., 2019). In contrast, the groundmass of eruptive products was variably crystalline. While pyroclasts were microcryst-free, the microcryst content of lava groundmass was more variable (between 20 and 90 vol%) (Schipper et al., 2015, 2019). Porosity in lavas ranged from 0 to 48% (Schipper et al., 2015, 2019), while pumices generated during the initial sub-Plinian activity showed values between 62 and 92% (Pistolesi et al., 2015). Tephra emitted during the hybrid eruption phase was mainly pumiceous, with porosities between 32 and 67% and a tube-like fabric (Schipper et al., 2013). Bombs and lavas erupted during the hybrid phase showed complex and heterogeneous juxtaposition of textures and volatile trace element depletion trends, which were indicative of outgassing processes occurring between the shallow conduit (<200 m, so above the laccolith) and the surface environment (Paisley et al., 2019a). Bomb textures contained breccias and tuffisite veins with variable size, porosity, degree of oxidation, and welding (Fig. 1 C-E). Although texturally distinct, both recorded the development of permeable pathways for gas (Paisley et al., 2019b). These textures were also preserved in situ in the vent area, where dome-like lava bodies with high-density fracture networks can be observed.

3. Methods

3.1. Video analyses

To help constrain magma ascent dynamics, we estimate gas and tephra venting velocities and the number of actively venting fractures from videos of the eruptive plumes. We re-analyze videos that were originally analyzed by Schipper et al., (2013); a 5-min nighttime video collected on January 4, 2012, and a 25-min daytime video collected on January 10, 2012. Venting characteristics likely evolved over the

duration of the hybrid phase of this eruption, but this is the only time span for which we have video. The videos were collected at $0.04\,\mathrm{s}$ frame rates with a stationary Canon XF105 camera 3.5 km from the vent (Fig. 3). Correlating the dome in the videos with satellite imagery indicates that each pixel corresponds to $\sim 0.2\,\mathrm{m}$.

In the nighttime video we manually track 20 individual ballistic particles, which can be clearly identified due to their incandescence, from frame-to-frame (Fig. 3C). Since these particles may be moving slower than the surrounding gas flow, they provide only a rough lower bound on gas venting velocities. We do not attempt to account for motion perpendicular to the camera frame, which may cause particle speeds to be underestimated. In the daytime video we manually track the locations of actively venting surface fractures over time (Fig. 3B). We also estimate gas and tephra venting velocities using an optical flow feature tracking method (Sun et al., 2008) that tracks brightness patterns in groups of pixels between frames. We again do not attempt to account for motion perpendicular to the camera frame, but take several steps to isolate regions of the velocity field that best represent actual venting velocity. We analyze only a sub-frame of the video that encompasses the near-vent region (Fig. 3B). We also consider only the vertical component of velocities, since the initial venting from most fractures is primarily vertical before wind shear and eddies introduce significant horizontal components. We then only keep vertical velocities above a threshold of 3 m/s (blue vectors, Fig. 3B), which we infer is a minimum feasible venting velocity based on visual assessment of this video and based on the manually tracked ballistic particles from the nighttime video. We finally examine only upper quantiles of the thresholded vertical velocity values (75th and 99th quantiles, Fig. 3A). We note that while these steps help isolate the parts of the velocity field in the video that best represent venting velocities, in some frames nearvent parts of the eruptive plumes are obscured, and even where nearvent parts of eruptive plumes are visible the video will only capture the flow exterior which will be slower than the cross-sectionally averaged flow velocity.

3.2. Model of magma ascent in the conduit

We turn to models of magma ascent in a conduit to examine the role of outgassing through magmatic fractures in facilitating eruption of lowporosity lava at Cordón Caulle volcano. We do not attempt to evaluate every process occurring during magma ascent, but rather focus on those most relevant to quantifying overall gas flux through the conduit and adjacent wall rock. We also do not attempt to address the complicated and often poorly constrained mechanics governing when and where fractures form and how they evolve (Gonnermann and Manga, 2005; Farquharson et al., 2017). Instead, we assume a fracture count and solve for the fracture onset depth and depth-varying fracture widths that could allow sufficient outgassing to permit the observed eruption of low-porosity lava. We can then compare the results of this modeling to other observational constraints on fracture network geometry and to gas-and-tephra venting velocities. Full model details are provided in the appendix; here we provide a conceptual summary, discuss important assumptions, and show the main governing equations.

We use a steady state model. Some amount of unsteadiness is evidenced by temporal variation in gas-and-tephra venting and intermittent explosions observed at Cordón Caulle volcano and other silicic eruptions (Michaut et al., 2013; Schipper et al., 2013; Johnson et al., 2014). Additionally, at least over small spatial scales, fracture network structures are likely not steady due to intermittent fracture formation and welding, as suggested by textures and diffusion timescales (Castro et al., 2014; Paisley et al., 2019a, 2019b). However, at Cordón Caulle volcano the observed relative stability in lava extrusion rate and gas/tephra plume height over timescales of months, as well as the stability of large surface fractures over at least timescales of hours, suggest that a steady-state approximation may be reasonable for at least some temporal and spatial scales.

We assume a conduit geometry that is cylindrical at depth with a vent radius that flares outward approaching the surface (Fig. 1). This flare allows for flow divergence as would occur in a growing lava dome/flow. We assume the conduit extends 3 km beneath the surface, which is consistent with the shallower estimates of magma storage depth (Castro et al., 2013; Jay et al., 2014). We do not consider any potential influence of the shallow laccolith (Castro et al., 2016) since it was emplaced prior to much of the hybrid phase we focus on, but note that it could have still been interacting with subsequent ascending magma as a source or sink for heat, melt, and/or volatiles. However, we expect this would probably not fundamentally change our results, since most outgassing occurs within the upper several hundred meters of the conduit (e.g., Figs. 4, 8). A dike-like magma pathway that only focuses to a narrow conduit at shallow depths has also been proposed at Cordón Caulle volcano (Castro

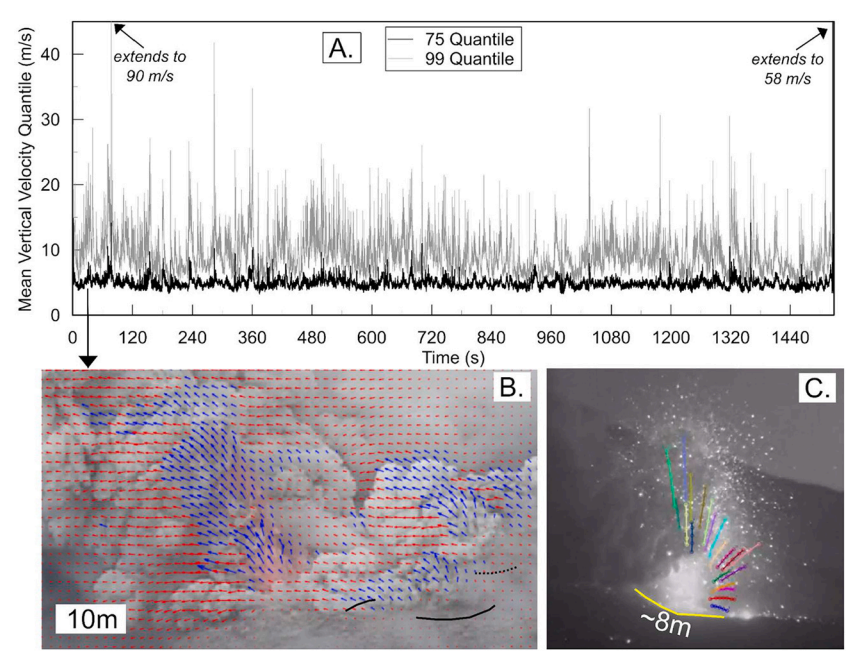


Fig. 3. Video analysis of surface fracture venting during the hybrid phase of the 2011 Cordón Caulle volcano eruption. A. Optical flow data from video on January 10, 2012, showing quantiles between each video frame pair (every 0.04 s) of all vertical velocities above a 3 m/s threshold. B. Velocity field showing a relatively intense burst (at 40s, black arrow) from a fracture near the edge of the vent. Blue vectors highlight regions that exceed the 3 m/s vertical velocity threshold, solid black lines show mostly visible surface fractures, and dashed black lines show partly obscured surface fractures. C. Trajectories of ejected ballistic particles during a burst captured in nighttime footage on January 4, 2012, along with the source fracture location (yellow line). (For interpretation of the references to colour in this figure legend, the reader is referred to the web version of this article.)

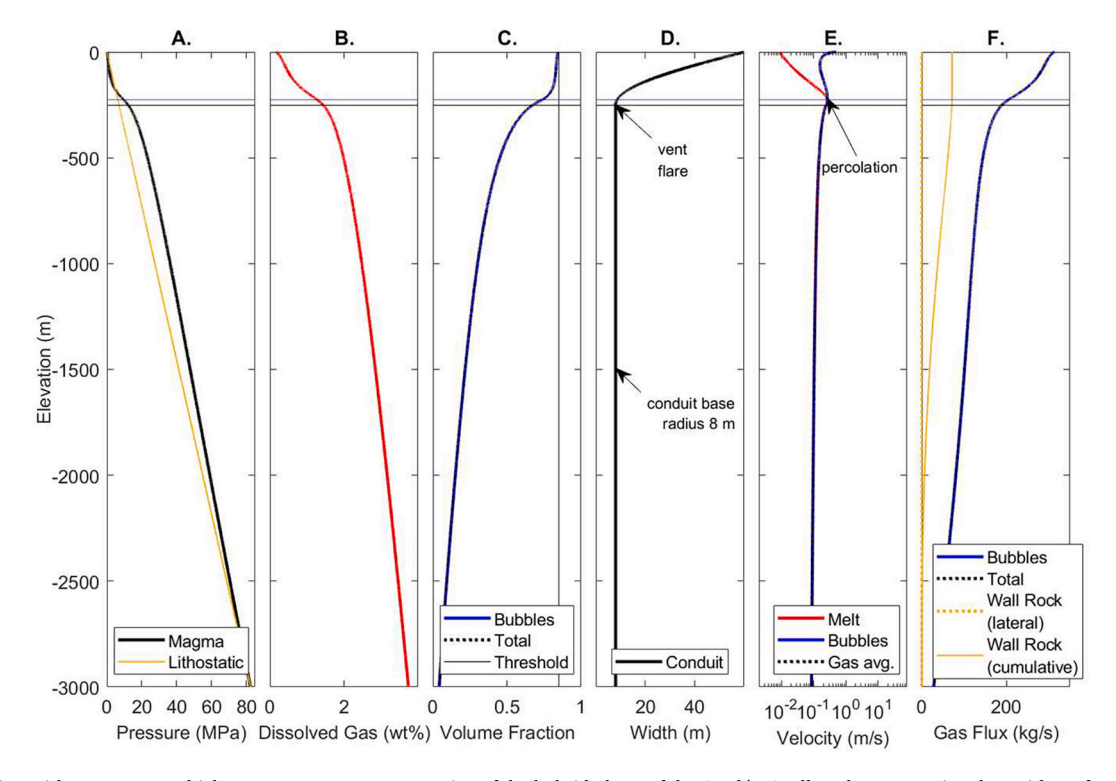


Fig. 4. Simulation with parameters which we assume are representative of the hybrid phase of the Cordón Caulle volcano eruption, but without fractures. Parameter values are from Table 1, except vent porosity threshold $φ_{vent}$ which is left at 85%. A. Pressure. B. Dissolved gas (H₂O). C. Gas volume fractions in bubbles $φ_b$ as well as the prescribed total porosity threshold $φ_{thresh}$. D. Widths of the conduit (2r). E. Velocity of melt u_m , gas in bubbles u_{gb} , and gas average u_g . F. Vertical gas fluxes

through bubble networks, as well as lateral gas flux to the wall rock q_w and cumulative wall rock gas flux (which indicates the additional amount of gas flux that would be occurring through the conduit in absence of losses to the wall rock). In all plots the horizontal black line indicates vent flare depth and the blue line indicates percolation depth. (For interpretation of the references to colour in this figure legend, the reader is referred to the web version of this article.)

et al., 2013); but we also expect this would not fundamentally change our results due to the predominance of shallow outgassing.

We use a 1D model, assuming a Poiseuille flow profile to account for viscous drag between the ascending magma and the conduit walls. We note that radial variations in strain rate and magma properties (viscosity, porosity, etc.) might contribute to several potentially important effects not considered here. Strain rate can directly influence permeability of bubble networks, effective magma viscosity, and fracture formation, all of which can also influence each other (Gonnermann and Manga, 2003; Llewellin and Manga, 2005; Okumura et al., 2009, 2010). For example, it has been proposed that shear localization near the conduit walls could enhance outgassing along the conduit margins but not necessarily allow outgassing in the center of the conduit (Shea et al., 2012; Okumura et al., 2013). However, several mechanisms could act to balance this. Less efficient gas escape in the center of the conduit could lead to higher gas overpressures there, which could promote fracturing and hence more efficient gas flow in the center of the conduit. Additionally, depending upon the flow regime, decreasing porosity due to extensive compaction and/or welding could increase magma viscosity in the conduit margins (Llewellin and Manga, 2005) and thus redistribute shear strain more evenly.

Our model allows relative motion between melt and gas phases (Fig. 1) but assumes that pressure in both phases is the same at a given depth (Yoshida and Koyaguchi, 1999; Kozono and Koyaguchi, 2009a; Degruyter et al., 2012). This assumption cannot be accurate in detail, and neglects some potentially important processes. Pressure gradients between fractures and the adjacent melt would generally be needed to drive gas flow into the fractures, and could also drive localized fragmentation at fracture walls (Forte and Castro, 2019) that contributes to fracture growth and introduces tephra to the fractures (Saubin et al., 2016). Such pressure differences would also drive fractures to widen/

propagate or narrow/close (Anderson, 2017).

We include both viscous and inertial drag forces on the melt resulting from gas flow through bubble and fracture networks. We include hysteresis-dependent bubble network permeability (Gonnermann et al., 2017) during magma compaction. We neglect particles (ash and/or larger pyroclasts) within the gas phase. For small volume fractions and sizes of particles (Stokes number <1), particle-laden gasses will essentially behave like gasses with increased density (Marble, 1970), and thus produce higher drag force for a given speed. We also include gas loss to adjacent permeable wall rock, which is parameterized based on the difference between the conduit pressure and lithostatic pressure as well as an assumed host rock permeability and pressure diffusion length scale (Jaupart and Allègre, 1991). While this is highly simplified, by testing a wide range of host rock permeabilities we can explore conditions that could permit a significant amount of gas loss through host rock.

We assume a uniform temperature of 900 °C, within the inferred storage temperature range (Castro et al., 2013; Jay et al., 2014) and matching the temperature of advancing lava as inferred from rheological models (Farquharson et al., 2015). We note that cooling during magma ascent could significantly increase melt viscosity (Hess and Dingwell, 1996). However, for the later stages of the eruption the surrounding wall rock would already be hot, and heat lost to the wall rock and from gas expansion would be partially offset by heat generated from crystallization and viscous dissipation (Burgisser and Degruyter, 2015).

We assume equilibrium gas exsolution. Diffusion timescales (length²/diffusivity) for rhyolite melt with a bubble spacing of $\sim 10^{-5}$ – 10^{-3} m (Saubin et al., 2016) and diffusivity of $\sim 10^{-7}$ – 10^{-5} m²/s (Ni and Zhang, 2008) will be $\sim 10^{-5}$ - 10^{1} s. Our simulations involve magma ascent rates of $\sim 10^{-2}$ - 10^{0} m/s (conduit ascent timescales of $\sim 10^{3}$ – 10^{5} s), which suggests the equilibrium solubility assumption is reasonable. We neglect volatile species other than H₂O, as H₂O is the

largest volumetric gas component at shallow depths in this system (Schipper et al., 2019). We also neglect crystals, given the relatively small crystal contents (<5 vol% phenocrysts and up to 25 vol% microcrysts) of near-vent Cordón Caulle volcano lava (Castro et al., 2013; Schipper et al., 2015) and limited constraints on microcryst formation depth. Crystal contents of up to 25 vol% could increase effective magma viscosity by roughly a factor of two (Caricchi et al., 2007), though this is small compared to the multiple orders of magnitude increases resulting from volatile exsolution (Hess and Dingwell, 1996). Crystallization can also drive volatile exsolution, but decompression will be the primary driver of exsolution at shallow depths in an ascending magma column with relatively small crystal contents (Westrich et al., 1988).

3.3. Model governing equations and boundary conditions

Gas mass conservation in the vertical (z, positive upward with origin at ground level as in Fig. 1) direction is given by:

$$\frac{\mathrm{d}}{\mathrm{d}z} \left(\rho_{gu_{\underline{x}}} A \phi \right) = -A(1 - \phi) \rho_m u_m \frac{\mathrm{d}C_d}{\mathrm{d}z} - q_w \tag{1}$$

where u_g is average gas velocity (including both bubbles and fractures),

 u_m is melt velocity, ϕ is total porosity or gas volume fraction (including both bubbles and fractures),A is conduit cross-sectional area, ρ_g is gas density, ρ_m is melt density, C_d is dissolved volatile mass fraction, and q_w is gas mass flux through the conduit wall parameterized based on the difference between the conduit pressure and lithostatic pressure (Jaupart and Allègre, 1991) (appendix A6). Melt mass conservation (assuming constant ρ_m) is given by:

$$\rho_m \frac{\mathrm{d}}{\mathrm{d}z} (u_m A(1 - \phi)) = A(1 - \phi) \rho_m u_m \frac{\mathrm{d}C_d}{\mathrm{d}z}$$
 (2)

Gas momentum conservation is given by:

$$A\phi \rho_{g_{\underline{u}_{\underline{s}}}} \frac{\mathrm{d}\underline{u}_{\underline{s}}}{\mathrm{d}z} = -A\phi \left(\frac{\mathrm{d}P}{\mathrm{d}z} + \rho_{\underline{s}}g\right) - F_{mg} \tag{3}$$

where F_{mg} is the total drag force per unit length between melt and gas (in both bubble and fracture networks, section 3.4), P is pressure (assumed to be the same in melt and gas), and g is gravitational acceleration. Drag between gas and conduit walls is neglected due to being negligible compared to other drag forces (Degruyter et al., 2012). Melt momentum conservation is given by:

$$A(1-\phi)\rho_m u_m \frac{\mathrm{d}u_m}{\mathrm{d}z} = -A(1-\phi)\left(\frac{\mathrm{d}P}{\mathrm{d}z} + \rho_m g\right) + F_{mg} - F_{mw} \tag{4}$$

where F_{mw} is drag force per unit length between melt and the conduit walls, given by the Poiseuille flow approximation $F_{mw} = 8A\mu_m u_m/r^2$ for conduit radius r and magma viscosity μ_m .

We prescribe total mass flux at the base of the conduit $q_{initial}$, pressure at the top of the conduit P_{atm} , and pressure at the base of the conduit P_{base} , then solve for a base conduit radius that satisfies these conditions. Conduit base pressure or mass flux could also be used as free parameters (Mastin, 2002), but here we solve for radius as it is more poorly constrained than the other two parameters at Cordón Caulle volcano.

3.4. Model partitioning of gas between bubble networks and fractures

We next need to obtain F_{mg} , which depends on effective magma column permeability. Without introducing physical equations governing the opening and evolution of fractures, it is necessary to either prescribe fracture network geometries empirically, or to set some other criterion, such as a target effective permeability of the magma column, and then calculate fracture depths and widths that produce this criterion. There are some constraints on fracture network geometry and permeability structure from the morphology and permeability of tuffisites in

pyroclasts and dissected conduits (Castro et al., 2014; Heap et al., 2019), but the general distribution of these properties with depth are poorly known.

We thus prescribe porosity thresholds, which provides the most direct way to have simulations that produce eruption of low-porosity lava. We enforce that porosity at any depth stays beneath 85%, because porosities significantly higher than 85% are rare in silicic lavas (Gonnermann et al., 2017) due to the fact that brittle fragmentation would typically occur by this point (Polacci et al., 2004). In detail, fragmentation depends upon factors such as strain rate and bubble overpressure (Gonnermann, 2015), but a porosity threshold is a practical approximate fragmentation criterion that can produce comparable results to commonly used strain-rate or overpressure criteria in permeable conduit magma ascent models (Degruyter et al., 2012). Above a prescribed compaction threshold depth, we smoothly taper the 85% porosity threshold down towards a prescribed vent porosity threshold (Fig. 6).

We then solve for values of F_{mg} that keep porosity from exceeding the prescribed porosity threshold. For an assumed fracture count and fracture wall roughness, we next solve for fracture onset depth, depth-varying fracture width, and depth-varying partitioning of gas flux between fractures and bubble networks that produces these values of F_{mg} by balancing drag pressure between fractures and bubble networks. We neglect the dependence of lateral gas flux on lateral gas pressure gradients and permeability (which is potentially anisotropic) (Farquharson and Wadsworth, 2018). This is justified by the assumption that where bubble network permeability is low enough to hinder lateral gas flux into the modeled vertical fractures, a feeder network of fractures could facilitate this lateral gas flux (Fig. 1).

4. Results

4.1. Tephra venting characteristics

Over the 25 min daytime video, continuous tephra venting occurred from 4 to 8 distinct surface fractures with a combined visible length of 20–40 m (Fig. 3). Additional active surface fractures are inferred to be present from the plume structure but are obscured behind the dome and/or eruptive plume. Some fractures were not active over the whole timespan, consistent with previous analysis (Schipper et al., 2013), and the location of active fractures shows a net southward migration over this video. There are also intermittent changes in the venting intensity at each fracture, often as bursts ejecting lava bombs or other visible ballistic particles and/or incandescent lava fountaining. These bursts often correspond to a decrease then subsequent increase in plume brightness suggestive of changing tephra content. The bursts are somewhat irregular, ranging from 5 to 20 s long and occurring at 20–60 s intervals.

An example optical-flow-derived velocity field from the daytime video is shown in Fig. 3B. The highest vertical velocities typically occur near surface fracture openings; the rest of the velocity field represents wind and plume turbulence, much of which is excluded by our 3 m/s vertical velocity threshold. Fig. 3A shows quantiles of the thresholded vertical velocities over time. The 99th quantile exhibits isolated values up to 88 m/s but is typically between 5 and 25 m/s (Fig. 3A). We expect this quantile provides the best lower bound estimate on gas and tephra venting velocity, since it captures velocities in jet-like regions of eruptive plumes near surface fracture openings where these regions are visible. However, in many frames these regions are obscured, which we expect causes many of the lower velocities in the timeseries. The 75th quantile yields more consistent but slower velocities between 5 and 10 m/s (Fig. 3A). This quantile often captures upward motion of turbulent eddies in higher parts of the eruptive plumes, so we expect it is less representative of venting velocities than the 99th quantile but include it as a more conservative lower bound.

We can also compare the optical flow velocities to the 20 manually tracked incandescent ballistic particles from nighttime video, which

provide a rough lower bound on gas venting velocity since they might be moving slower than the surrounding gas flow. The particles have an average vertical velocity of 13 ± 2 m/s and a maximum vertical velocity of 33 m/s, which suggests that the higher values of the 99th quantile velocities from the optical flow measurements are reasonable. Overall, the limitations of the available data preclude a detailed resolution of gas and tephra venting velocities, but suggest that these velocities are consistently at least 5 m/s, and are likely greater than tens of m/s over much of the recorded time.

4.2. Magma ascent dynamics without fractures

Fig. 4 shows an example simulation with our reference parameters that are assumed to be most representative of the hybrid phase of the Cordón Caulle volcano eruption, but with vent porosity threshold ϕ_{vent} left at 85%. Here exsolution occurs beneath the base of the conduit. Overpressure begins driving some gas loss to the wall rock at ~3000 m depth, though not in sufficient amounts to keep porosity from increasing significantly during magma ascent. Porosity reaches the percolation threshold of 74% (Gonnermann et al., 2017) at 226 m depth, shortly after the prescribed vent flare depth of 250 m. Following the onset of percolation, gas begins flowing faster than the adjacent melt, which allows porosity to increase less rapidly. Magma pressure begins decreasing more rapidly, becoming sub-lithostatic at ~180 m depth at which point gas loss to the wall rock ceases. Porosity reaches 84% at the vent, just beneath the prescribed fragmentation threshold of 85% and much higher than typical observed lava porosities at Cordón Caulle volcano of 0 to 48% (Schipper et al., 2015, 2019). By the time magma reaches the vent, about 18% of its gas has been lost to the wall rock.

We note that over certain regions of the conduit, the magma

overpressure (relative to lithostatic pressure) exceeds several MPa, which could be enough to fracture the wall rock (Unwin et al., 2021). However, overpressures depend strongly on the assumed value of conduit base pressure P_{base} and the lithostatic pressure profile P_{lith} , which in reality would generally increase more rapidly with depth than our profile due to increasing rock density with depth. We do not consider wall rock fracturing, but note that it could change the effective conduit geometry, result in external tuffisite vein emplacement, and increase the effective permeability of the nearby wall rock to facilitate additional gas loss. Our simulations with higher values of k_w (discussed later) in combination with the relatively short pressure diffusion length scale we assume do provide an approximate means of accounting for increased gas loss due to a highly fractured wall rock.

To gain a sense for how low the value of lava porosity could feasibly become without enhanced fracture-mediated outgassing, we can consider different parameter choices that would promote more efficient outgassing through the wall rock and bubble networks. Fig. 5 shows an example simulation with our reference parameters changed so that initial mass flux $q_{initial}$ has been reduced to 10^2 kg/s, wall rock permeability k_w has been increased to $10^{-12}\,\mathrm{m}^2$, and ϕ_{vent} has been left at 85% (a side by side comparison is shown in Fig. A2). Here gas loss to the wall rock is sufficient to keep porosity from increasing significantly until a depth of ~400 m, when the rate of gas exsolution begins exceeding the rate of gas loss. Magma pressure becomes sub-lithostatic at ~250 m depth, at which point gas loss to the wall rock ceases. Pressure becoming sub-lithostatic at shallow depths is actually a feature of all of our simulations, and indicates an important limitation to wall rock mediated outgassing. Porosity reaches the percolation threshold at 204 m depth, after which the rate of porosity increase begins slowing down substantially. From ~150 to 60 m depth, porosity actually decreases by about

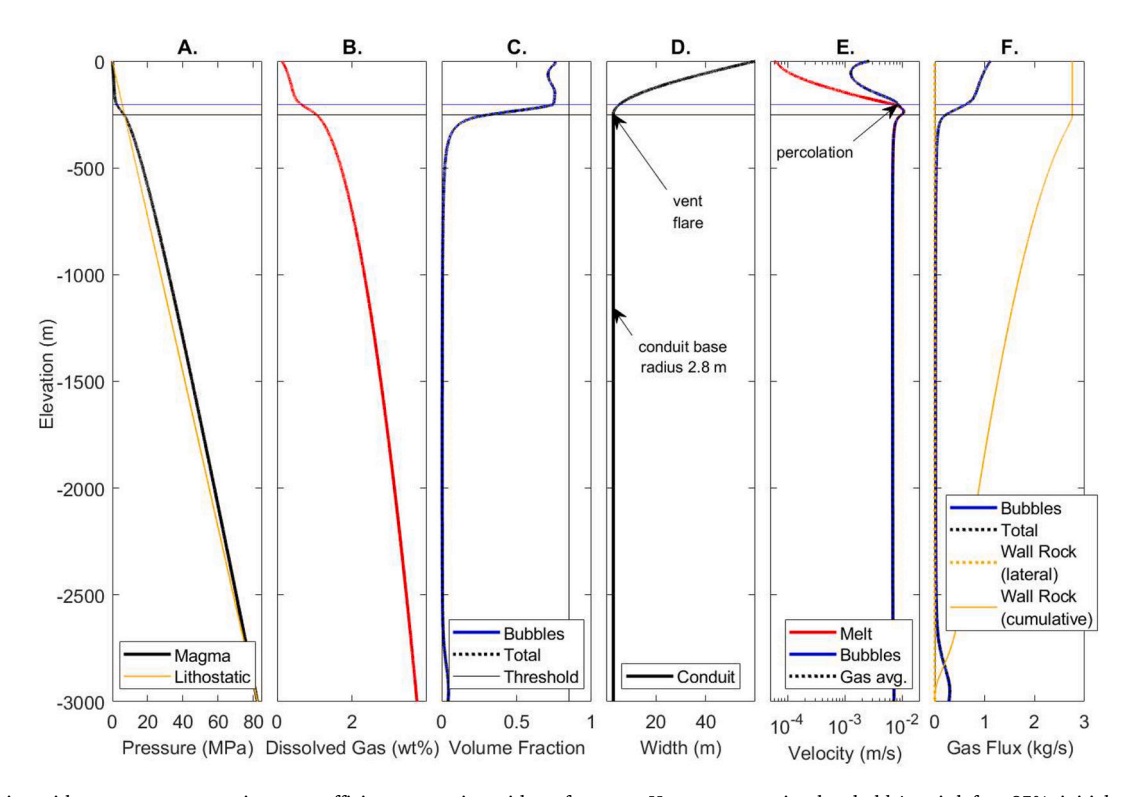


Fig. 5. Simulation with parameters promoting more efficient outgassing without fractures. Here vent porosity threshold ϕ_{vent} is left at 85%, initial mass flux $q_{initial}$ is reduced to 10^2 kg/s, wall rock permeability k_w is increased to 10^{-12} m², and other parameter values are from Table 1. A. Pressure. B. Dissolved gas (H₂O). C. Gas volume fractions in bubbles ϕ_b as well as the prescribed total porosity threshold ϕ_{thresh} . D. Widths of the conduit (2r). E. Velocity of melt u_m , gas in bubbles u_{gb} , and gas average u_g . F. Vertical gas fluxes through bubble networks, as well as lateral gas flux to the wall rock q_w and cumulative wall rock gas flux (which indicates the

additional amount of gas flux that would be occurring through the conduit in absence of losses to the wall rock). In all plots the horizontal black line indicates vent flare depth and the blue line indicates percolation depth. (For interpretation of the references to colour in this figure legend, the reader is referred to the web version of this article.)

4%. However, porosity then begins increasing again, despite the hysteresis that allows bubble network permeability to remain elevated during compaction and the flow divergence induced by an increasing conduit radius. By the time magma reaches the vent, 29% of its gas has been lost to the wall rock, and porosity reaches 76%. Thus even under conditions much more favorable for outgassing via permeable bubble networks and wall rock, low porosity lava is still not produced.

4.3. Magma ascent dynamics with fractures

Fig. 6 shows an example simulation with our reference parameters where vent porosity threshold φ_{vent} is set to 25%, a typical value of observed lava porosities at Cordón Caulle volcano (a side by side comparison is shown in Fig. A2). Here we assumed 10 conduit-spanning fractures of equal width, which is very roughly consistent with the configuration of actively venting fractures at the lava dome surface seen in video. However, fracture density and size distribution likely vary over depth (e.g., Fig. 1). We note that the exact characteristics of fracture networks obtained in our model will depend strongly on fracture count, as well as the somewhat arbitrarily prescribed functional forms of vent flare geometry and porosity threshold and the assumed fracture wall roughness.

In this simulation exsolution still occurs beneath the base of the conduit, and magma overpressure begins driving some gas loss to wall rock at a depth of $\sim\!2000$ m. Porosity reaches the percolation threshold of 74% at 226 m depth and continues increasing. Porosity then reaches the prescribed threshold value of 80% at a depth of 185 m, at which point fractures are introduced. The fractures need to widen rapidly to accommodate increasing gas flux, and by $\sim\!160$ m depth more gas flux is occurring through fractures than through the bubble network. By the

time magma reaches the vent, 18% of its gas has been lost to the wall rock, and 99.9% of the remaining gas flux is flowing through fractures. Fracture width and gas velocity in fractures both reach their maximum values at the vent of 7 cm and 54 m/s, respectively.

4.4. Overview of magma ascent under different eruptive conditions

To examine results more systematically, we run simulations over a range of different model parameter combinations and plot several important properties from each simulation. Fig. 7 shows fracture width and gas velocity in fractures at the vent, Fig. 8 shows the depths of percolation onset and fracture formation, and Fig. 9 shows the percentage of gas flux occurring through fractures at the vent and lost to the wall rock during magma ascent.

We note that there are some cases where our numerical methods do not find solutions meeting the prescribed porosity thresholds, which could be due to either numerical stiffness or to non-existence of solutions. A rigorous analysis of the existence of solutions for this highly non-linear model is beyond the scope of this work, but we discuss the implications below. We also note that some simulations result in gas velocities in fractures that approach the sound speed for pure H2O vapor at 900 °C of 840 m/s. This could produce choked flow conditions, for which our model will not be accurate. Although including particles in our simulations would decrease the gas velocities predicted, a particleladen gas could have appreciably slower sound speeds. We thus conservatively suggest that any solutions resulting in gas velocities greater than several hundred m/s should be considered potentially unphysical or unrealistic. We also note that due to the nonlinearity of the model it is possible that multiple solutions sometimes exist, though testing suggests that this is not the case for parameters of interest.

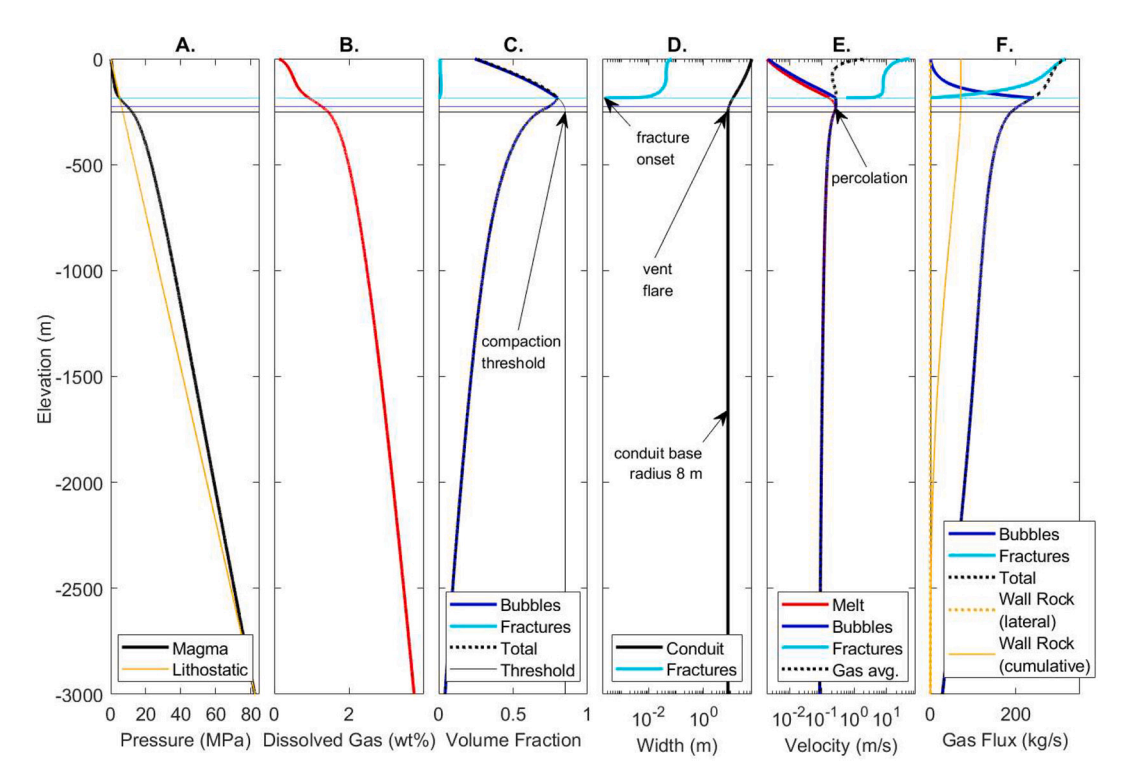


Fig. 6. Simulation with parameters which we assume are representative of the hybrid phase of the Cordón Caulle volcano eruption, including fractures as are required to produce a vent porosity $φ_{vent}$ of 25%. All parameter values are from Table 1. A. Pressure. B. Dissolved gas (H₂O). C. Gas volume fractions in bubbles $φ_b$ and in fractures $φ_f$, as well as the prescribed total porosity threshold $φ_{thresh}$. D. Widths of the conduit (2r) and fractures w_f . E. Velocity of melt u_m , gas in bubbles u_{gb} , gas in fractures u_{gf} , and gas average u_g . F. Vertical gas fluxes through bubble networks and fractures, as well as lateral gas flux to the wall rock q_w and cumulative wall rock

gas flux (which indicates the additional amount of gas flux that would be occurring through the conduit in absence of losses to the wall rock). In all plots the horizontal black line indicates vent flare depth, the blue line indicates percolation depth, and the light blue line indicates fracture onset depth. (For interpretation of the references to colour in this figure legend, the reader is referred to the web version of this article.)

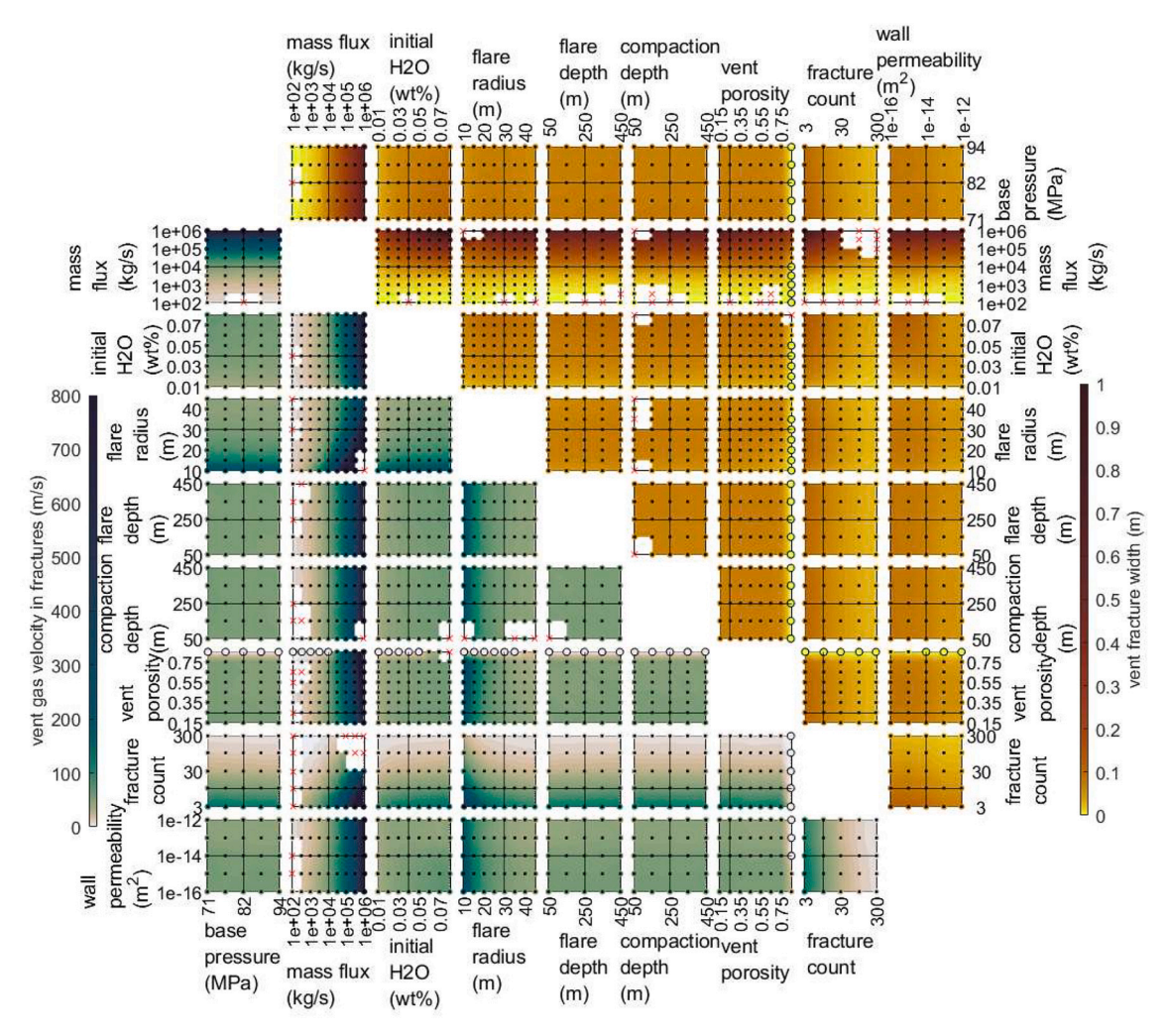


Fig. 7. Vent gas velocity in fractures and vent fracture width for different parameter values. In each plot all parameters except the two being varied are fixed to default values, which are indicated by black lines. Red crosses indicate simulations where the numerical methods did not find a solution meeting the porosity thresholds, black circles indicate solutions with no fractures, and black dots indicate solutions with fractures. Colored contours are linearly interpolated between simulations. Estimated gas-and-tephra venting velocities at Cordón Caulle volcano are on the order of 10–100 m/s, and estimated widths of major surface fractures are on the order of 0.1–1 m. (For interpretation of the references to colour in this figure legend, the reader is referred to the web version of this article.)

The main finding of this parameter search is that in all regions of the parameter space where our numerical methods find solutions that meet the prescribed porosity thresholds, magmatic fractures are required except where vent porosity is allowed to reach 85% (Fig. 7). Additionally, in most of the parameter space the majority of the overall gas flux at shallow depths needs to occur through fractures (Fig. 9). This parameter search thus indicates that a significant amount of enhanced outgassing (e.g., via fractures) would be required to produce the erupted lava at Cordón Caulle volcano which had 0 to 48% porosity (Schipper et al., 2015, 2019).

We can also compare these simulations to gas vent velocities inferred from video, which are on the order of tens of meters per second. However, we emphasize that we are considering only order-of-magnitude comparisons due to the limitations of venting velocity estimates from video, the limited time over which video is available, the assumption of pure gas rather than a gas-particle mixture in our simulations, and the assumptions of fracture network geometry and wall roughness in our simulations. Our simulations can produce velocities on the order of tens of meters per second for many parameter combinations except those involving mass fluxes substantially outside the inferred range of $10^4 \hbox{--} 10^5 \ \mbox{kg/s}$, vent flare radii of less than $\sim\!20$ m, vent porosities greater than $\sim\!75\%$, or fracture counts greater than $\sim\!30$ (Fig. 7).

We can also approximately compare our simulations to constraints

from tuffisites, which indicate fracture widths on the order of tens of cm (Heap et al., 2019; Paisley et al., 2019b) and fracture depth extents of at least 200 m beneath the vent (Schipper et al., 2013; Castro et al., 2016; Paisley et al., 2019b). Our simulations can produce fracture widths on the order of tens of cm for most parameter combinations except those involving mass fluxes substantially outside the inferred range of 10^4 – 10^5 kg/s or vent porosities greater than ~75% (Fig. 7). Fracture onset depth in our simulations depends largely on the prescribed porosity threshold compaction depth and the prescribed vent flare depth (Fig. 8), and both parameters have minimal impact on other observables (Fig. 7). Setting both depth parameters to values beneath \sim 200 m will produce fracture onset depths beneath 200 m. However, we note that the fracture onset depth in our simulations only provides a minimum bound on the possible depth extent of fractures, which in turn means that our simulations do not rule out shallower vent flare depths or compaction onset depths.

4.5. Details on the effects of different eruptive conditions on magma

In this section we address the effects of different model parameters in more detail. We vary the conduit base (or shallow reservoir) pressure P_{base} from 71 to 94 MPa, extending both below and above expected

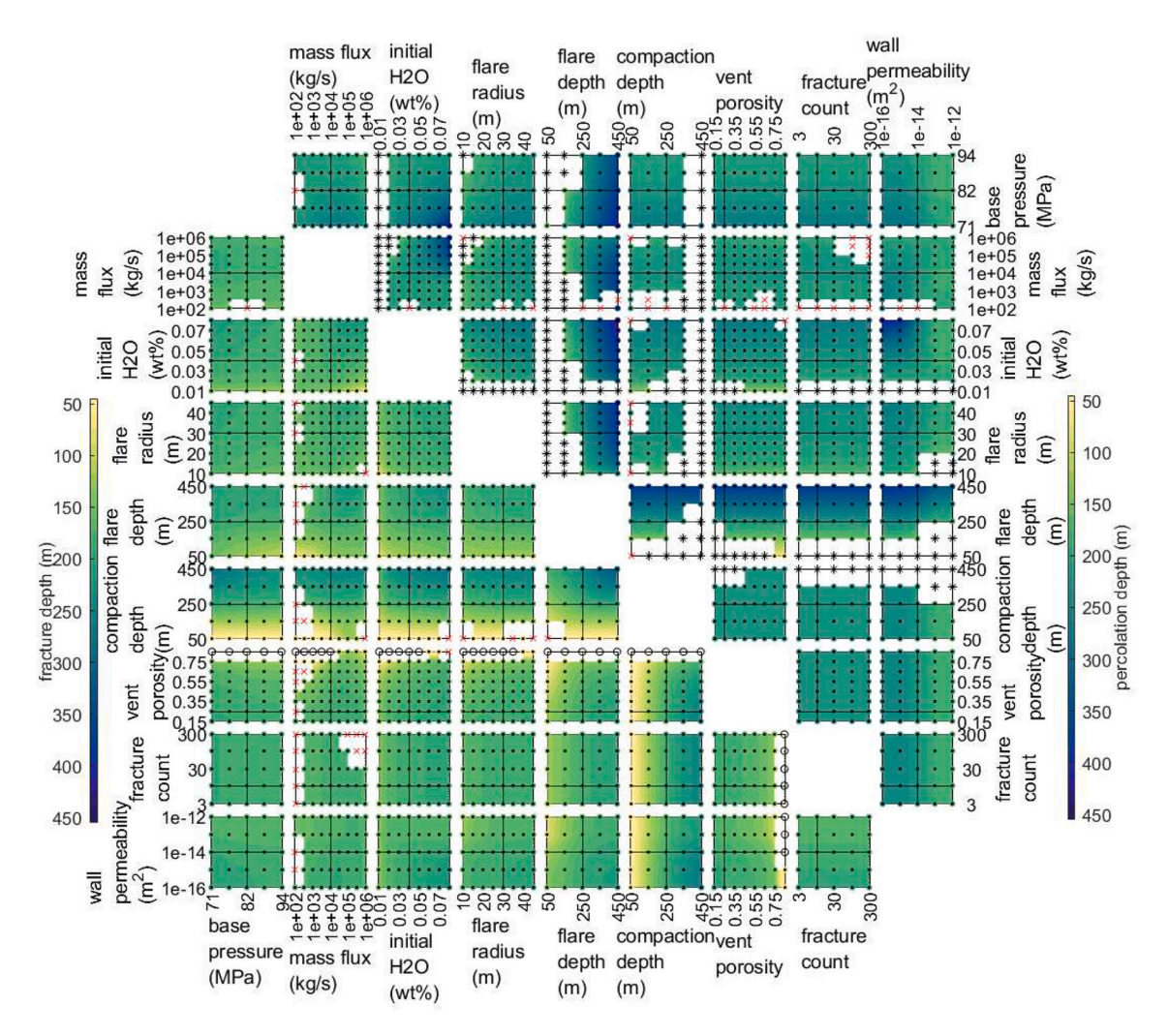


Fig. 8. Depths of fracture onset and bubble network percolation onset for different parameter values. In each plot all parameters except the two being varied are fixed to default values, which are indicated by black lines. Red crosses indicate simulations where the numerical methods did not find a solution meeting the porosity thresholds, black circles indicate solutions with no fractures, black stars indicate solutions with fractures where the percolation threshold was never reached, and black dots indicate solutions with fractures where the percolation threshold was reached. Colored contours are linearly interpolated between simulations. Petrologically inferred tuffisite depths at Cordón Caulle volcano (which provide a lower bound on fracture depths) are up to 200 m. (For interpretation of the references to colour in this figure legend, the reader is referred to the web version of this article.)

lithostatic pressure of 82.5 MPa (for a crustal density of 2800 kg/m³). Results near the ends of this range may be unrealistic, as significant overpressures would drive fracturing of the wall rock (Unwin et al., 2021) and significant underpressures might not hold the conduit open. We also note that in these simulations mass flux is prescribed independently of conduit base pressure; if conduit base radius were instead prescribed then conduit base pressure would be a dominant control on mass flux (Mastin, 2002) and have a larger impact on simulation results. Increasing conduit base pressure causes shallower percolation and fracture onset depths (Fig. 8). Increasing overpressure also drives more gas loss to the wall rock, particularly at higher wall rock permeabilities, and thus reduces the percentage of gas flux in fractures (Fig. 9).

We vary mass flux $q_{initial}$ from 10^2 to 10^6 kg/s, encompassing the 10^4 – 10^5 range of previous estimates for the hybrid/effusive phase (Bertin et al., 2015). Increasing mass flux increases the velocity of gas in fractures at the vent and increases vent fracture width (Fig. 7). Increasing mass flux also increases the percentage of gas flux in fractures, while generally decreasing the percentage of gas lost to the wall rock (Fig. 9). At mass fluxes $<10^3$ kg/s, solutions are found inconsistently, though we expect this is largely due to numerical issues rather than the non-existence of solutions. For mass fluxes above 10^4 kg/s, fractures are needed even to keep vent porosity at 85%. For mass fluxes

above $10^5~{\rm kg/s}$, gas velocity in fractures approaches or exceeds the sound speed for a particle-laden gas, suggesting such simulation results may be unphysical or unrealistic.

We vary initial H_2O contents $C_{initial}$ from 1 to 8 wt%, encompassing the inferred storage value of 3.9 wt% (Jay et al., 2014). Increasing initial volatile contents increases the velocity of gas in fractures at the vent and increases vent fracture widths (Fig. 7). Increasing initial H_2O contents also causes deeper percolation and fracture onset depths (Fig. 8), as well as deeper exsolution depths (not shown). Increasing initial H_2O contents generally decreases the percentage of gas flux in fractures but increases gas loss to the wall rock (Fig. 9). For initial H_2O contents >5 wt%, fractures are needed even to keep vent porosity at 85%.

We vary vent flare radius r_{flare} from 10 to 50 m, encompassing the estimated dome radius of 25–40 m (Schipper et al., 2013) since this parameter is meant to account roughly for the flow divergence that could occur in the lava dome/flow. We note that combinations involving large flare radii and short flare depths could produce significant radial components of velocity that would violate the unidirectional flow assumption in our model. The main impact of increasing vent flare radius is to decrease the velocity of gas in fractures at the vent (Fig. 7). Given that increasing vent flare radius thus generally facilitates more efficient outgassing, it is somewhat counterintuitive that fractures are

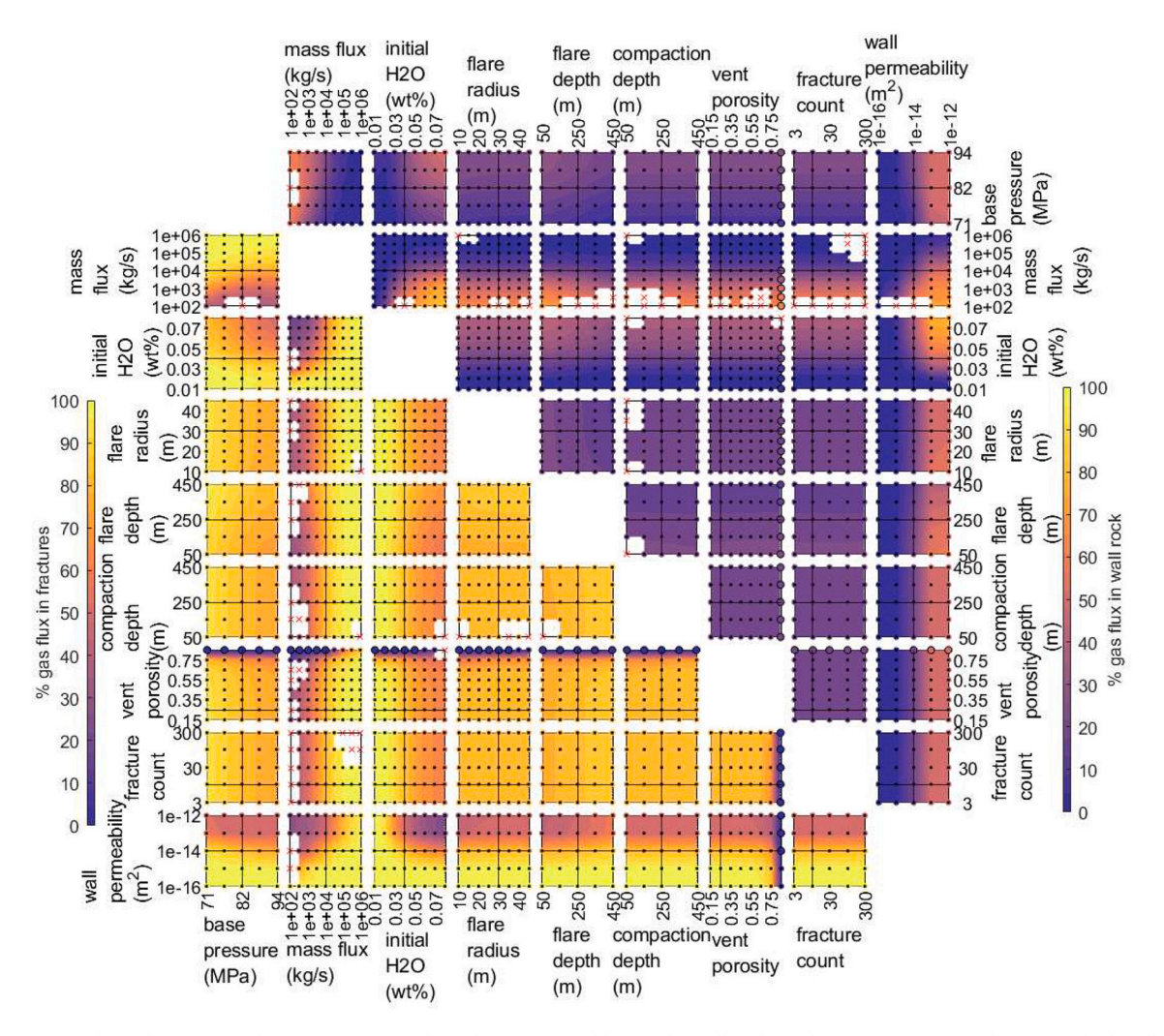


Fig. 9. Percent of total gas flux (at vent elevation) occurring through fractures and lost to the wall rock for different parameter values. In each plot all parameters except the two being varied are fixed to default values, which are indicated by black lines. Red crosses indicate simulations where the numerical methods did not find a solution meeting the porosity thresholds, black circles indicate solutions with no fractures, and black dots indicate solutions with fractures where the percolation threshold was reached. The wall rock gas flux value used is the cumulative loss, as is plotted in Figs. 4, 5, and 6. (For interpretation of the references to colour in this figure legend, the reader is referred to the web version of this article.)

needed even to keep vent porosity at 85% for flare radii of 40 m or larger, but not for smaller radii. We attribute this finding largely to the chosen reference values of vent flare depth and porosity threshold compaction depth.

We vary vent flare depth z_{flare} and porosity threshold compaction depth $z_{compact}$ from 50 to 450 m, encompassing petrologic bounds on tuffisite depths of >200 m (Schipper et al., 2013; Castro et al., 2016; Paisley et al., 2019b). These parameters primarily influence fracture formation depth and percolation onset depth (Fig. 8). In cases where the vent flare depth is shallower than the porosity threshold compaction depth, porosity reaches the prescribed threshold before exceeding the bubble network percolation threshold (Fig. 8), which means that no gas flow occurs through the bubble networks. We expect these simulations are not realistic since there would be no mechanism to efficiently route gas into fractures. A very dense fracture network could serve this purpose, but is not explicitly considered in our modeling. However, we expect the relation between percolation onset and vent flare depth suggests that flow divergence plays an important role in facilitating fracture-mediated outgassing.

We vary prescribed magma porosity at the vent ϕ_{vent} between 15 and 85%, with 85% serving as an approximate brittle fragmentation criterion (Polacci et al., 2004). Lava porosities at Cordón Caulle volcano ranged from 0 to 48% (Schipper et al., 2015, 2019), but the lowest end

member values are not representative of the flow as a whole. Additionally, we note that the porosity-permeability relations used here may not be accurate for porosities much lower than 20% (Gonnermann et al., 2017), since due to the inefficiency of permeable flow in low porosity bubble networks, further compaction might occur primarily by localized fracturing/fragmentation and welding. Increasing vent porosity does not have a large impact on simulation results until vent porosity approaches \sim 75%. At this point increasing vent porosity decreases the velocity of gas in fractures at the vent, decreases vent fracture widths, and decreases the percentage of gas flux in fractures (Figs. 7, 9). At vent porosities of 85%, fractures are not needed except for mass fluxes >10 4 , initial H₂O contents >5 wt%, or vent flare radii >40 m.

We vary fracture count N_f from 3 to 300. The number of active large surface fractures inferred from Cordón Caulle volcano video is approximately 10, but fracture density may vary with depth, and a higher density of smaller fractures may be required to efficiently feed gas into a few larger fractures (e.g., Fig. 1) (Gonnermann and Manga, 2005). Increasing fracture count decreases gas velocity in fractures at the vent and decreases vent fracture widths (Fig. 7), but does not appreciably impact the percentage of gas flux in fractures (Fig. 9). For combinations with higher mass fluxes ($> \sim 10^5$ kg/s) and larger fracture counts ($> \sim 30$), solutions are not found. In these cases we expect solutions do not exist because the width of each fracture is limited by the number of

fractures present (for a given conduit width), and for the large wall roughness scale we assume, narrow fractures are not able to facilitate efficient outgassing. This is also why we do not show solutions with fracture counts >300, for which solutions often do not exist. However, this does not indicate that higher fracture densities are not possible, since fracture widths and wall roughness are likely variable.

We vary wall rock permeability k_w from 10^{-16} to 10^{-12} m². This encompasses the range of typical shallow crustal permeabilities (Manning and Ingebritsen, 1999) and also the range of tuffisite fill permeabilities which is relevant since early pyroclast breccia will be acting as effective wall rock for much of the eruption (Heap et al., 2019). Increasing wall rock permeability primarily decreases the percentage of gas flux in fractures and increases the percentage of gas lost to the wall rock (Fig. 9). High wall rock permeabilities combined with high initial H₂O contents or low mass flux can result in up to 82% of gas being lost to the wall rock, but gas losses are usually <40% (Fig. 9).

5. Discussion

5.1. Role of magmatic fractures in facilitating hybrid eruption at Cordón Caulle volcano

Other studies have suggested that magmatic fracturing and/or fragmentation were involved in the Cordón Caulle volcano eruption and are required to explain particular textural and geochemical observations (Castro et al., 2014), but the importance of such processes on overall eruption mechanics has been poorly constrained. Our simulations demonstrate that outgassing through permeable bubble networks and conduit wall rock (Eichelberger et al., 1986) could not have permitted the extrusion of low-porosity silicic lava that occurred during the later hybrid phase of the eruption (Fig. 7), and that a significant amount of enhanced outgassing needs to have occurred by some other mechanisms. We then show that outgassing through magmatic fracture networks that are consistent with available constraints on fracture depths and widths (from analysis of tuffisites) can allow sufficient enhanced outgassing to facilitate the observed eruption of low-porosity lava and match gas-andtephra venting velocities obtained from video analysis at Cordón Caulle volcano. Demonstrating that magmatic fractures can explain these observations does not rule out other scenarios that could result in enhanced outgassing, such as the occurrence of conduit-spanning brittle fragmentation and a gas-dominated flow regime beneath an effusively erupting magma plug (Wadsworth et al., 2020), but indicates that such scenarios are not necessary to allow a hybrid or effusive eruption over a certain range of mass fluxes.

We can gain additional insight from considering the progression of the Cordón Caulle volcano eruption sequence, which began as fully explosive and only transitioned to hybrid once mass flux decreased beneath $\sim 10^5$ kg/s (Bertin et al., 2015; Coppola et al., 2017; Jay et al., 2014). In our simulations, for mass fluxes $> \sim 10^5$ kg/s erupting low porosity lava with outgassing through magmatic fractures would require gas velocities exceeding the sound speed for a particle-laden gas, indicating such scenarios are unphysical or unrealistic. These unrealistic gas velocities suggest that a mass flux of $\sim 10^5$ kg/s is around the limit at which fracture-mediated outgassing could have facilitated a hybrid or effusive eruption, as opposed to a fully explosive eruption. Furthermore, it is notable that the Cordón Caulle volcano eruption transitioned from fully explosive to hybrid around this threshold of $\sim 10^5$ kg/s, despite our simulations indicating that fully explosive behavior could be sustained down to mass fluxes as low as 10 kg/s without enhanced outgassing. That the eruption transitioned to hybrid behavior around this 10⁵ kg/s threshold suggests that magmatic fractures developed in such a way as to facilitate the transition close to the threshold where transition was possible. Finally, our finding that outgassing through magmatic fractures is still required to enable eruption of low porosity lava for mass fluxes as low as 10 kg/s is consistent with observations that hybrid eruptive behavior with tephra venting continued approaching the end of the Cordón Caulle volcano eruption, despite decreasing inferred mass flux (Jay et al., 2014; Coppola et al., 2017).

5.2. Implications for effusive eruptions more generally

While we have focused primarily on simulations of the hybrid phase of the Cordón Caulle volcano eruption, our model should be able to inform other silicic eruptions given appropriate choices of conduit geometry, mass flux, reservoir pressure, and magma properties. The simulations in Fig. 7 do not consider a full range of parameter combinations that might be relevant for other eruptions, but cover a wide enough range of parameters to permit some extrapolation. The finding that fractures are not required to keep porosity beneath an approximate fragmentation threshold of 85% except where mass flux is $>10^4$ kg/s suggests that enhanced outgassing (beyond permeable bubble networks and/or wall rock) is not necessarily required to prevent fully explosive eruptions at mass fluxes <10⁴ kg/s. However, effusive eruption of lava with porosities approaching 85% is uncommon (Gonnermann et al., 2017), and our simulations show that enhanced outgassing (e.g., via magmatic fractures) is required to produce lava with porosities of 75% or less down to mass fluxes as low as 10 kg/s. The eruption record shows that there are effusive components in most silicic eruptions with magma ascent rates less than $\sim 1-10$ cm/s, which corresponds to mass fluxes less than $\sim 10^3 - 10^5$ kg/s (Cassidy et al., 2018). Our results thus suggest that enhanced outgassing may be required to explain the effusive component of most intermediate mass flux eruptions ($\sim 10-10^5$ kg/s). Additionally, our simulations indicate that over most of this range of mass fluxes, magmatic fractures can facilitate the required amount of enhanced outgassing to facilitate hybrid or effusive behavior without needing to invoke additional outgassing mechanisms (Wadsworth et al., 2020).

Another important question is under what conditions effusive eruptions (and/or explosive-effusive transitions) can occur. Previous models of permeable magma ascent that did not consider fractures have demonstrated that mass flux is a dominant control on whether effusive eruptions can occur (Kozono and Koyaguchi, 2009b; Degruyter et al., 2012), which is roughly consistent with the eruption record (Cassidy et al., 2018). However, the overlapping ascent rates inferred between explosive and effusive eruptions in the eruption record (Cassidy et al., 2018) suggest mass flux is not the only relevant parameter, and have even been used to argue against outgassing as the mechanism driving explosive-effusive transitions (Wadsworth et al., 2020). Our results suggest that magmatic fractures need to be considered to obtain a more accurate understanding of the transition between explosive and effusive activity, as there is a multiple order of magnitude range in mass fluxes $(\sim 10-10^5 \text{ kg/s})$ over which either explosive or hybrid/effusive eruptions could occur depending upon how much outgassing occurs through magmatic fractures (as well as other eruptive conditions).

In the absence of caldera collapse, mass flux will typically decrease over the course of a sustained eruption as the reservoir pressure driving magma ascent decreases (Huppert and Woods, 2002), making transitions from explosive to hybrid or effusive behavior generally more likely as an eruption progresses. However, other parameters could also evolve over the course of a sustained eruption. In particular, our simulations show that a widening vent can make fracture-mediated outgassing much more efficient and could thus potentially promote explosive-effusive transitions. Decreasing magma pressure as an eruption progresses could decrease conduit and/or vent width. Alternately, erosion could increase vent width during explosive phases of an eruption (Mitchell, 2005), and also during hybrid activity as indicated by the larger amounts of oxidized lithic fragments in bombs ejected during later times in the Cordón Caulle volcano eruption (Paisley et al., 2019b). Additionally, once a hybrid or effusive eruption is ongoing a growing lava dome would also increase effective vent width. This dome growth could thus help promote stability of a hybrid/effusive eruptive phase, although explosive dome collapse events indicate that a growing lava dome alone does not ensure full stability.

The importance of magmatic fractures emphasizes the need to develop a better understanding of the formation and evolution of fracture networks in ascending magma. Such an understanding is important for determining both what controls explosive-effusive transitions and what drives unsteady venting during hybrid eruptions. Additional work is also needed to address the possibility of producing hybrid/effusive eruptions with conduit-spanning brittle fragmentation and a gas dominated flow regime at depth (Wadsworth et al., 2020), as opposed to our model of a melt-and-fracture dominated flow regime. We are not aware of any observations or analysis that necessitate a gas dominated flow model for hybrid/effusive eruptions, and our simulations suggest this would not be necessary except possibly at mass fluxes greater than $\sim 10^4$ kg/s, but conduit-scale modeling has not yet been conducted to understand the mechanics of such a scenario. It is possible that early stages of lava extrusion occurring alongside or following a primarily explosive eruptive phase involve a gas-dominated flow regime, but that this transitions to the melt-and-fracture dominated flow we envision for sustained hybrid/effusive eruptions.

6. Conclusions

Our model of magma ascent in a conduit, combined with constraints from petrologic and video data, show that outgassing through permeable bubble networks and/or wall rock would not be sufficient to generate the observed flux of dense, gas-poor rhyolitic lava erupted during the later phases of the 2011–2012 Cordón Caulle volcano eruption. However, enhanced outgassing through magmatic fractures can facilitate the observed dense lava production and is consistent with constraints on fracture network geometries inferred from textural and geochemical analysis of tuffisites as well as with gas-and-tephra venting velocities inferred from video analysis.

Exploration of a range of conditions relevant to many silicic eruptions reveals that outgassing through permeable bubble networks and wall rock generally cannot generate lava at the low porosities typically observed. However, there is a wide range of conditions over which gas escape through fractures could permit hybrid/effusive eruption of dense lava. We thus infer that outgassing through fractures likely plays an important role in many hybrid/effusive silicic eruptions, and in facilitating explosive-effusive transitions. Our results highlight the importance of considering fractures both in magma ascent models and when interpreting the eruption record, as well as the need to develop a better understanding of magmatic fractures.

Appendix A. Appendix

A.1. Conduit radius and porosity threshold

Conduit radius is given by (Figs. 3, 4):

$$r = r_{base}$$
 if $z < z_{flare}$ (A1)

$$r = r_{flare} + \left(r_{flare} - r_{base}\right) \sin\left(\frac{z\pi}{-2z_{flare}}\right) \text{ if } z \ge z_{flare}$$
(A2)

where conduit flare radius r_{flare} and conduit flare depth z_{flare} are prescribed, and the value of conduit base radius r_{base} that meets the prescribed pressure boundary conditions is solved iteratively (appendix A7). This choice of function ensures that conduit radius and its derivative with respect to depth are both continuous.

Porosity thresholds ϕ_{thresh} are given by (Fig. 6):

$$\phi_{thresh} = \phi_{max} \text{ if } z < z_{compact}$$
(A3)

$$\phi_{thresh} = \phi_{vent} + (\phi_{vent} - \phi_{max}) \sin\left(\frac{\pi z}{-2z_{compact}}\right) \text{ if } z \ge z_{compact}$$
(A4)

where maximum porosity ϕ_{max} , vent porosity ϕ_{vent} , and porosity threshold compaction depth $z_{compact}$ are all prescribed. This choice of function ensures

Data availability

Video footage was collected by HT on behalf of the BBC, and data was obtained courtesy of the BBC. Codes are available upon request.

Declaration of Competing Interest

None

Acknowledgements

We thank Álvaro Amigo for providing data and discussion of Cordón Caulle volcano. We thank Ben Finney and the BBC for loan of the video camera and use of footage. We thank Editor Sonia Calvari, three anonymous reviewers, and USGS internal reviewer Kyle Anderson for constructive suggestions. This work was a part of the 2019 Cooperative Institute for Dynamic Earth Research (CIDER) 2019 summer program in Berkeley, CA, USA, supported by NSFEAR1135452; we thank the organizers Mohabbat Ahmadi, Bruce Buffett, the program organizing committee as well as many other participants for discussion and feedback. HT acknowledges a Royal Society University Research Fellowship. HMG was supported by NSF EAR1824252. PR was supported by NSF EAR1823122. EL was supported by NSF EAR1654588. Any use of trade, firm, or product names is for descriptive purposes only and does not imply endorsement by the U.S. Government.

CRediT author statement

Josh Crozier: Conceptualization, Methodology, Writing - original draft. Samantha Tramontano: Conceptualization, Methodology, Writing - original draft. Pablo Forte: Conceptualization, Writing - original draft. Sarah Jaye C: Oliva: Conceptualization, Writing - original draft. Helge M. Gonnermann: Conceptualization, Writing - original draft. Einat Lev: Conceptualization, Writing - original draft. Michael Manga: Conceptualization, Writing - original draft. Madison Myers: Conceptualization, Writing - original draft. Erika Rader: Conceptualization, Methodology. Philipp Ruprecht: Conceptualization. Hugh Tuffen: Writing - original draft, Methodology. Rebecca Paisley: Methodology. Bruce F Houghton: Conceptualization. Thomas Shea: Conceptualization. C Ian Schipper: Methodology. Jonathan M Castro: Methodology.

that the porosity threshold and its derivative with respect to depth are both continuous.

A.2. Partitioning of gas flow between fractures and bubble networks

We assume no fractures are present when $\phi < \phi_{thresh}$, so gas flow initially only occurs through bubble networks ($F_{mg} = F_{mgb}$). If ϕ approaches ϕ_{thresh} we require that F_{mg} takes on whatever value is required such that $d\phi/dz = d\phi_{thresh}/dz$ in the governing equations. This is implicitly invoking the presence of fractures to increase the effective permeability of the magma column such that ϕ_{thresh} is not exceeded.

For an assumed fracture count, we calculate fracture widths and the gas partitioning between bubble networks and fractures that produce the required values of F_{mv} (if any such partitioning exists):

$$F_{mg} = F_{mgb}(u_{gb}, \phi_b) + F_{mgf}(u_{gf}, \phi_f) \tag{A5}$$

where u_{gb} and u_{gf} are gas velocities in bubble networks and fractures, respectively. Gas volume fractions in bubble networks ϕ_b and fractures ϕ_f can be expressed as $\phi_b = A_b/A$ and $\phi_f = A_f/A$, for cross sectional areas in bubble networks A_b and fractures A_f . Because gas volume fraction in bubbles and fractures is related by $\phi_b + \phi_f = \phi_f$, there are three unknown variables in this expression: u_{gb} , u_{gf} , and ϕ_f . We need two additional equations to close this system. The second equation enforces mass conservation of gas:

$$\phi u_g = \phi_b u_{gb} + \phi_f u_{gf} \tag{A6}$$

For the third equation, we need a way to relate gas drag forces between the bubble networks and fractures. The most realistic approach would be to introduce both vertical and lateral mass and momentum balance equations governing gas flow through fractures and gas flow in/out of fractures, analogous to classical dual-porosity models for fractured media used in hydrogeological models (Gerke and van Genuchten, 1993). However, this would require additional assumptions about fracture growth and properties that are currently poorly constrained. Here, owing to the high permeability of bubbly magma and fractures, we assume that lateral gradients in pressure will remain small, meaning that pressure gradients in both fractures and the bubbly magma will be similar, and largest in the vertical direction. We thus make the approximation that drag pressure is equal between gas in fractures and bubble networks

$$\frac{F_{mgb}}{A_b} = \frac{F_{mgf}}{A_f} \tag{A7}$$

By neglecting inertia, the pressure gradients in both the bubble networks and fractures will be consistent with the solution to the governing eqs.

A.3. Bubble network drag force

We use Darcy-Forchheimer drag for force per unit length of gas flowing through bubble networks (Rust and Cashman, 2004; Degruyter et al., 2012):

$$F_{mgb} = \left(\frac{\mu_g}{k_1} + \frac{\rho_g}{k_2} |u_{gb} - u_m|\right) A \phi_b (1 - \phi_b) (u_{gb} - u_m) \tag{A8}$$

where μ_g is gas viscosity. Bubble network permeability is a function of bubble network porosity relative to the melt (not including fractures) $\phi_{br} = \phi_b/(\phi_b + (1 - \phi))$. This relation depends upon the compaction and growth history of the bubble network. We use the equation for Darcy permeability k_1 from percolation theory (Blower, 2001; Gonnermann et al., 2017):

$$k_1 = k_{min}$$
 if $\phi_{hirt} \le \phi_{crit}$ (A9)

$$k_1 = b(\phi_{br} - \phi_{crit})^n \left(\frac{\phi_{br}}{(1 - \phi_{br})}\right)^{2/3} \text{ if } \phi_{br} \ge \phi_{hist} \text{ and } \phi_{hist} > \phi_{crit}$$
(A10)

$$k_1 = b(\phi_{br}(y) - \phi_{crit})^n \left(\frac{\phi_{br}}{(1 - \phi_{br})}\right)^{2/3} \left(\frac{\phi_{br}}{\phi_{br}(y)}\right)^{n_{compact}} \text{ if } \phi_{br} < \phi_{hist} \text{ and } \phi_{hist} > \phi_{crit}$$
(A11)

where k_{min} assigns small values ($< 10^{-14} \text{ m}^2$) that prevent numerical issues which arise if permeability is too small, ϕ_{crit} is the percolation threshold, ϕ_{hist} is the maximum porosity previously reached during ascent (defined as $\phi_{hist} = \max(\phi_{br}(y))$) for all y in the interval -L < y < z), and b, n, $n_{compact}$ are constants. We use values of b, n, $n_{compact}$ and ϕ_{crit} from Medicine Lake Volcano rhyolitic pumice (Gonnermann et al., 2017). For these values, once the percolation threshold has been exceeded, during compaction ($\phi_{br} < \phi_{hist}$) permeability at a given porosity will remain higher than during initial growth ($\phi_{br} \ge \phi_{hist}$) and will depend on ϕ_{hist} (Fig. A1). We note that although this expression was derived for compacting bubble networks, compacting welded material exhibits qualitatively similar hysteresis (Farquharson et al., 2017) but may follow a different functional form. We do not introduce a separate gas-melt Stokes drag regime at low porosities, since we found this had a negligible impact on our simulation results but increased computation times. Inertial permeability k_2 is given empirically:

$$k_2 = c_k k_1 + d_k \tag{A12}$$

where c_k and d_k are constants obtained empirically by fitting Medicine Lake Volcano rhyolitic pumice, but this relation also fits samples from other settings well (Gonnermann et al., 2017).

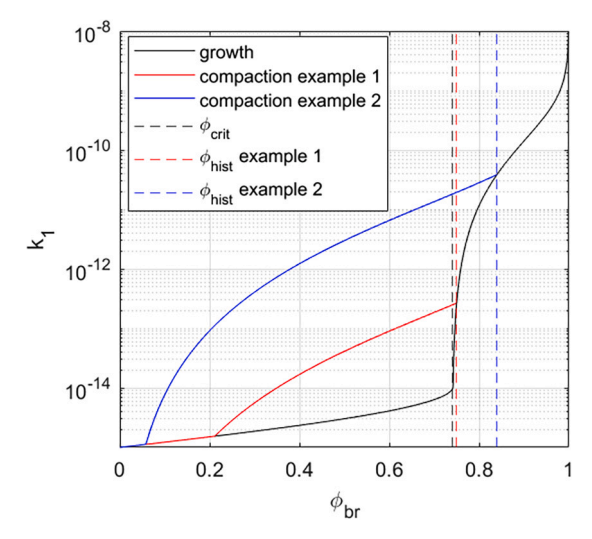


Fig. A1. Bubble network Darcy permeability as a function of porosity. The solid black line shows permeability during bubble growth, and the two colored lines show permeability during compaction starting from two example porosities.

A.4. Fracture drag force

Force per unit length between magma and gas in fractures is given by (Munson et al., 1994):

$$F_{mgf} = P_f \rho_g (u_{gf} - u_m) |u_{gf} - u_m| f_F = 2N_f L_f \rho_g (u_{gf} - u_m) |u_{gf} - u_m| f_F$$
(A13)

where P_f is fracture cross sectional parameter, which we use the assumption of thin fractures to approximate as $P_f = 2N_{fL_f}$ for number of fractures N_f and average fracture length L_f . For simplicity we assume that all fractures span the diameter of the conduit, so $L_f = \pi r/2$. The Darcy friction factor f_D is given by the laminar-turbulent approximation (Munson et al., 1994):

$$f_D = f_{D0} + f_D^*$$
 (A14)

where f_{D0} is the laminar Darcy friction factor, which we approximate as (Duan et al., 2012):

$$f_{D0} = 4N_f \frac{\mu_g}{\rho_g \left| u_{gf} - u_m \right| \sqrt{w_f L_f}} \frac{12}{\sqrt{w_f / L_f \left(1 + w_f / L_f \right) \left(1 - 192 / \pi^5 \left(w_f / L_f \right) \tanh \left(\pi L_f / 2 w_f \right) \right)}}$$
(A15)

where $\frac{\mu_g}{\rho_g |u_g - u_m| \sqrt{w_f L_f}}$ is the Reynolds number for the fracture length scale $\sqrt{A_f} = \sqrt{w_f L_f}$ and fracture width w_f . We approximate the turbulent Darcy friction factor f_D^* as (Duan et al., 2012):

$$f_D^* = 4N_f \left(3.6 \log_{10} \left(0.2047 \left(\frac{\epsilon}{\sqrt{w_f L_f}} \right)^{10/9} + 6.115 \frac{\mu_g}{\rho_g \left| u_{gf} - u_m \right| \sqrt{w_f L_f}} \right) \right)^{-2}$$
(A16)

where ϵ is fracture wall roughness height scale. The roughness height scale could vary with depth and fracture width and in general is not well constrained. Here we assume roughness height scale is a constant factor of the fracture length scale $\epsilon = c_\epsilon \sqrt{w_f L_f}$, for a prescribed fracture wall roughness height scale constant c_ϵ . We note that for thin fractures these roughness height scales can be greater than the actual fracture width, but this is not inconsistent given the parameterization in Eq. (A15). It might seem simpler to set $\epsilon = c_\epsilon w_f$, but for the friction parameterizations used this would result in drag force that does not decrease monotonically with increasing fracture width. We set c_ϵ to a relatively high value of 0.25. The high value provides an approximate way to account for flow resistance that would arise from complicated fracture networks geometries (rather than just contiguous parallel planes), and ensures that the hydraulic conductivity of fractures is not overestimated compared to bubble networks.

A.5. Magma properties

We use Henry's law for equilibrium water solubility:

$$S_w = c_{\chi} \sqrt{P}$$
 (A17)

where c_s is a saturation constant (Burnham and Jahns, 1962). We also introduce an additional minor amount of persistent exsolved gas that both approximates the presence of other gasses like CO_2 that would start exsolving beneath our model domain (Newman and Lowenstern, 2002; Schipper et al., 2019) and improves numerical stability. Dissolved water is then given by:

$$C_d = S_w \text{ if } S_w < C_{initial} - C_{permanent}$$
 (A18)

$$C_d = C_{initial} \text{ if } S_w \ge C_{initial} - C_{permanent}$$
 (A19)

where $C_{initial}$ is initial total water content and $C_{permanent}$ is the small amount of persistent gas (0.1 wt%). We use the ideal gas law for gas density:

$$\rho_g = \frac{P}{R_v T} \tag{A20}$$

where R_g is the specific gas constant for H_2O and T is temperature. We note that at greater depths within the conduit, exsolved H_2O will actually be a supercritical fluid with higher density than indicated by the ideal gas law. We assume constant density for the melt.

We assume constant and Newtonian gas viscosity. We use an empirical function for the Newtonian viscosity of hydrous leucogranitic melts (Hess and Dingwell, 1996):

$$\log_{10}(\mu_m) = -3.545 + 0.833 \ln(100C_d) + \frac{9601 - 2368\ln(100C_d)}{T - (195.7 + 32.25\ln(100C_d))}$$
(21)

The impact of bubbles on effective magma viscosity can be significant, though less than the multiple orders of magnitude arising from volatile exsolution (Hess and Dingwell, 1996). Additionally, the magnitude and sign of the impact of bubbles on effective magma viscosity depends on strain rate (Llewellin and Manga, 2005), which would make the effective magma viscosity non-Newtonian and inconsistent with our Poiseuille flow assumption. For simplicity we thus neglect the impact of bubbles on effective magma viscosity.

A.6. Gas flux through conduit walls

Mass flux of gas through the conduit walls/host rock is approximated as (Jaupart and Allègre, 1991):

$$q_w = 0 \text{ if } P \le P_{lith} \tag{A22}$$

$$q_{w} = 2\pi r_{c} \phi \frac{\rho_{g}}{\mu_{g}} min \left(\frac{k_{w}(P - P_{lith})}{L_{w}} \frac{k_{1}(P - P_{lith})}{r} \right) \text{ if } P > P_{lith}$$
(A23)

where k_w is wall rock Darcy permeability (assumed constant), k_1 is magma Darcy permeability (Eqs. (A9)-(A11)), L_w is an assumed wall rock pressure diffusion length scale, and P_{lith} is lithostatic pressure which we approximate assuming a uniform wall rock density ρ_w :

$$P_{lith} = -\rho_{w}gz \tag{A24}$$

The minimum condition ensures that excessive amounts of gas are not lost to the conduit walls when permeability of the magma column would be a limiting factor. When $\phi < 10^{-3}$ we downscale q_w to keep $\phi \ge 0$ during integration. This treatment of wall rock gas loss neglects inertial permeability, which is valid in the limit of slow lateral gas flow. Lateral gas velocity will decay approximately inversely with distance away from the conduit (as a simple radial mass conservation formulation would show), so the slow lateral gas flow assumption is likely valid except possibly very near the conduit. This approach additionally neglects overpressure-induced fracturing of conduit walls (Jaupart, 1998; Unwin et al., 2021), which could allow additional gas flow depending upon the size and spacing of these fractures and the permeability of any magmatic material that fills them. Lastly, the assumption of uniform wall rock density may underestimate lithostatic pressure (and hence overestimate wall rock gas loss) at depth if density increases with depth.

A.7. Numerical methods

We numerically integrate P_m , ϕ , and volatile flux (within the conduit, so excluding wall rock gas loss) q_v over depth starting from the base of the conduit. Integration is done with a modified version of MATLAB's ode23s stiff differential equation solver that stores variable histories and allows us to account for permeability hysteresis. All integration variables are scaled and shifted so that their attainable values range between one and two, and for all of the scaled integration variables we use an integration error tolerance per depth increment of 10^{-8} . Integration steps are informed by Jacobians (e.g., $(dP_m/dz)/dP_m$, $(dP_m/dz)/d\varphi$, and etc.) which we estimate using first order finite difference approximations with directionality and step sizes adjusted based upon the state of the integration variables to ensure stability. While we have chosen these integration methods based on extensive testing, the equations can be very stiff, so in some cases integrations do not complete due to numerical issues.

Within each integration step the linear system of governing equations (Eqs. (1)–(4)) are solved for dP_m/dz , $d\phi/dz$, du_m/dz , and du_g/dz . Above

depths where the chosen porosity threshold has been met (meaning fractures are present) we use MATLAB's fzero iterative nonlinear root finding algorithm to solve for the value of F_{mg} that meets the condition:

$$\frac{d\phi}{dz} = \frac{d\phi_{thresh}}{dz} + \chi e^{-\psi(\phi - \phi_{thresh})} \tag{A25}$$

within a tolerance of 10^{-37} m⁻¹, where χ and ψ are small constants (10^{-6} and 10^{-3} respectively) such that the exponential term enforces a gradual convergence to the threshold that increases numerical stability. We then use two nested applications of fzero to solve the system of three equations governing partitioning of gas flow between bubble networks and fractures for u_{gb} , u_{gf} , and ϕ_f , with a tolerance of 10^{-35} Pa on the pressure balance between bubble networks and fractures, and a tolerance of 10^{-35} N/m on the total gas drag force per unit length. For numerical stability we impose the limit that fractures cannot occupy >99% of the total porosity. In some cases even with all gas flow occurring through fractures a low enough value of F_{mg} cannot be reached to satisfy the porosity threshold, in which case we stop that integration.

To meet the atmospheric pressure condition at the top boundary, we use an alternating bisection/secant shooting method (which can increase convergence rates) to iteratively repeat integrations with different values of base conduit radius r_{base} . We set initial feasible bounds on r_{base} using Poiseuille flow calculations. We assume an acceptable solution has been reached when $P_{alm} < P_m < 2P_{alm}$ and -2 < z < 2. In some cases the shooting method does not converge to a solution because values of r_{base} that over and under-shoot the top boundary condition (or that do not satisfy the porosity threshold) are separated by less than our chosen threshold of 10^{-8} m. Where the shooting results of such cases were assessed in detail, there is no indication that further refinement of r_{base} would yield a solution. In such cases testing different tolerances elsewhere in the numerical methods also generally does not yield solutions, though we cannot guarantee that solutions do not exist. In all cases, for the values of r_{base} tested the cost functions appear to be monotonic (except where the porosity threshold is not met where cost is not defined), which suggests it is unlikely (though not impossible) that there are multiple solutions over the interval of r_{base} considered.

A.8. Additional figures

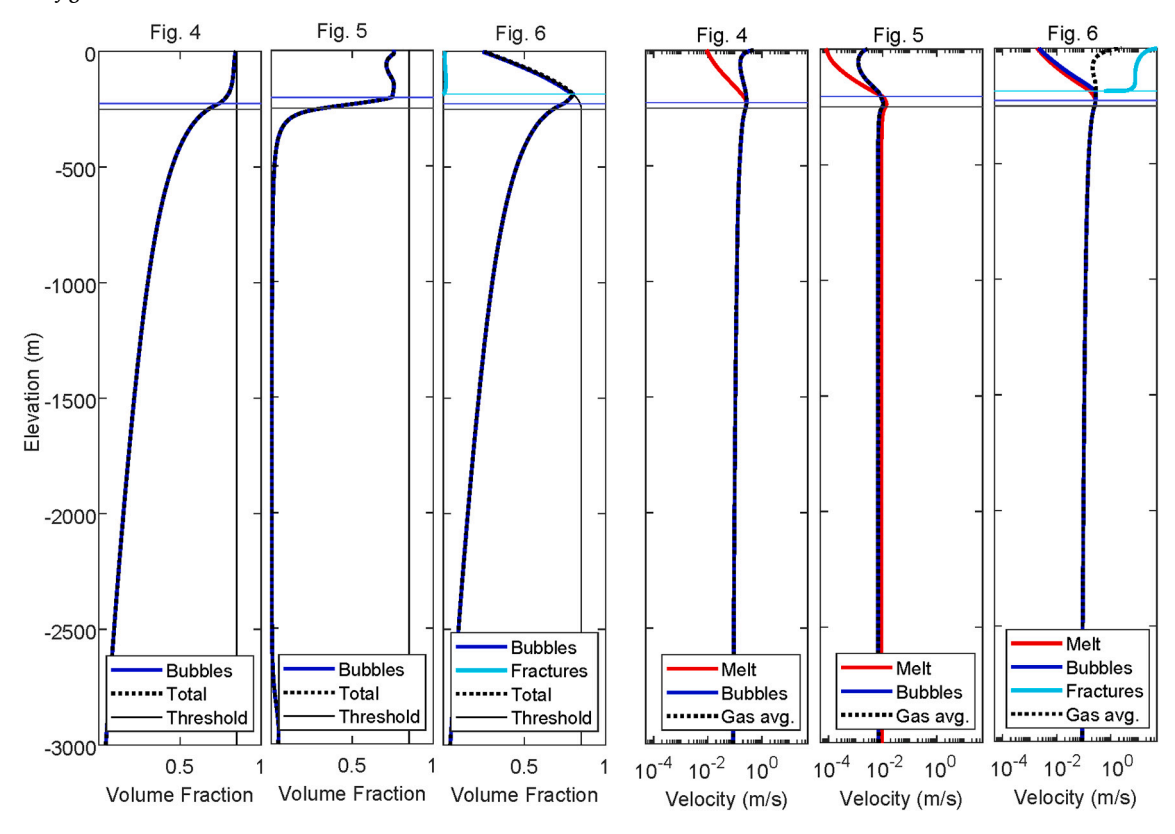


Fig. 42. Comparison of simulations in Fig. 4, Fig. 5, and Fig. 6. In the Fig. 4 simulation parameter values are from Table 1, except vent porosity threshold ϕ_{vent} which is left at 85%. In the Fig. 5 simulation vent porosity threshold ϕ_{vent} is left at 85%, initial mass flux $q_{initial}$ is reduced to 10^2 kg/s, wall rock permeability k_w is increased to 10^{-12} m², and other parameter values are from Table 1. In the Fig. 6 simulation all parameter values are from Table 1.

References

Allen, J., Simmon, R., 2012. Puyehue Cordón Caulle [WWW Document]. Nasa Earth Observatory. URL. https://earthobservatory.nasa.gov/images/77065/puyeh ue-corda3n-caulle (accessed 1.23.22).

Alloway, B.V., Pearce, N.J.G., Villarosa, G., Outes, V., Moreno, P.I., 2015. Multiple melt bodies fed the AD 2011 eruption of Puyehue-Cordón Caulle, Chile. Sci. Rep. 5, 17589. https://doi.org/10.1038/srep17589.

Anderson, T.L., 2017. Fracture Mechanics: Fundamentals and Applications. CRC Press. https://doi.org/10.1201/9781315370293.

Berlo, K., Tuffen, H., Smith, V.C., Castro, J.M., Pyle, D.M., Mather, T.A., Geraki, K., 2013. Element variations in rhyolitic magma resulting from gas transport. Geochim. Cosmochim. Acta 121, 436–451. https://doi.org/10.1016/j.gca.2013.07.032.

Bertin, D., Lara, L.E., Basualto, D., Amigo, Á., Cardona, C., Franco, L., Gil, F., Lazo, J., 2015. High effusion rates of the Cordón Caulle 2011–2012 eruption (Southern Andes) and their relation with the quasi-harmonic tremor. Geophys. Res. Lett. 42, 7054–7063. https://doi.org/10.1002/2015GL064624.

Black, B.A., Manga, M., Andrews, B., 2016. Ash production and dispersal from sustained low-intensity Mono-Inyo eruptions. Bull. Volcanol. 78, 57. https://doi.org/10.1007/ s00445-016-1053-0.

Blower, J.D., 2001. A three-dimensional network model of permeability in vesicular material. Comput. Geosci. 27, 115–119. https://doi.org/10.1016/S0098-3004(00) 00066-2.

Bonadonna, C., Pistolesi, M., Cioni, R., Degruyter, W., Elissondo, M., Baumann, V., 2015. Dynamics of wind-affected volcanic plumes: the example of the 2011 Cordón Caulle eruption, Chile. J. Geophys. Res. Solid Earth 120, 2242–2261. https://doi.org/ 10.1002/2014JB011478.

Burgisser, A., Degruyter, W., 2015. Magma ascent and degassing at shallow levels. In: Sigurdsson, Haraldur (Ed.), The Encyclopedia of Volcanoes, 2nd edition. Elsevier, pp. 225–236. https://doi.org/10.1016/B978-0-12-385938-9.00011-0.

Burnham, C.W., Jahns, R.H., 1962. A method for determining the solubility of water in silicate melts. Am. J. Sci. 260, 721–745. https://doi.org/10.2475/ajs.260.10.721.

Caricchi, L., Burlini, L., Ulmer, P., Gerya, T., Vassalli, M., Papale, P., 2007. Non-Newtonian rheology of crystal-bearing magmas and implications for magma ascent dynamics. Earth Planet. Sci. Lett. 264, 402–419. https://doi.org/10.1016/j.epsl 2007.09.032

Cassidy, M., Manga, M., Cashman, K., Bachmann, O., 2018. Controls on explosive-effusive volcanic eruption styles. Nat. Commun. 9, 2839. https://doi.org/10.1038/s41467-018-05293-3.

Castro, J.M., Cordonnier, B., Tuffen, H., Tobin, M.J., Puskar, L., Martin, M.C., Bechtel, H. A., 2012. The role of melt-fracture degassing in defusing explosive rhyolite eruptions at volcán Chaitén. Earth Planet. Sci. Lett. 333–334, 63–69. https://doi.org/10.1016/j.epsl.2012.04.024.

Castro, J.M., Schipper, C.I., Mueller, S.P., Militzer, A.S., Amigo, A., Parejas, C.S., Jacob, D., 2013. Storage and eruption of near-liquidus rhyolite magma at Cordón Caulle. Chile. Bull. Volcanol. 75, 702. https://doi.org/10.1007/s00445-013-0702-9

Castro, J.M., Bindeman, I.N., Tuffen, H., Schipper, C.I., 2014. Explosive origin of silicic lava: Textural and-H 2 O evidence for pyroclastic degassing during rhyolite effusion. Earth Planet. Sci. Lett. 405, 52–61. https://doi.org/10.1016/j.epsl.2014.08.012.

- Castro, J.M., Cordonnier, B., Schipper, C.I., Tuffen, H., Baumann, T.S., Feisel, Y., 2016.
 Rapid laccolith intrusion driven by explosive volcanic eruption. Nat. Commun. 7, 13585. https://doi.org/10.1038/ncomms13585.
- Coppola, D., Laiolo, M., Franchi, A., Massimetti, F., Cigolini, C., Lara, L.E., 2017. Measuring effusion rates of obsidian lava flows by means of satellite thermal data. J. Volcanol. Geotherm. Res. 347, 82–90. https://doi.org/10.1016/j. ivolgeores.2017.09.003.
- Degruyter, W., Bachmann, O., Burgisser, A., Manga, M., 2012. The effects of outgassing on the transition between effusive and explosive silicic eruptions. Earth Planet. Sci. Lett. 349–350, 161–170. https://doi.org/10.1016/j.epsl.2012.06.056.
- Delgado, F., 2021. Rhyolitic volcano dynamics in the Southern Andes: contributions from 17 years of InSAR observations at Cordón Caulle volcano from 2003 to 2020. J. S. Am. Earth Sci. 106, 102841 https://doi.org/10.1016/j.jsames.2020.102841.
- Delgado, F., Kubanek, J., Anderson, K., Lundgren, P., Pritchard, M., 2019.
 Physicochemical models of effusive rhyolitic eruptions constrained with InSAR and DEM data: a case study of the 2011-2012 Cordón Caulle eruption. Earth Planet. Sci. Lett. 524, 115736 https://doi.org/10.1016/j.epsl.2019.115736.
- Duan, Z., Yovanovich, M.M., Muzychka, Y.S., 2012. Pressure drop for fully developed turbulent flow in circular and noncircular ducts. J. Fluids Eng. 134 https://doi.org/ 10.1115/1.4006861.
- Eichelberger, J.C., Carrigan, C.R., Westrich, H.R., Price, R.H., 1986. Non-explosive silicic volcanism. Nature 323, 598–602. https://doi.org/10.1038/323598a0.
- Elissondo, M., Baumann, V., Bonadonna, C., Pistolesi, M., Cioni, R., Bertagnini, A., Biass, S., Herrero, J.-C., Gonzalez, R., 2016. Chronology and impact of the 2011 Cordón Caulle eruption, Chile. Nat. Hazards Earth Syst. Sci. 16, 675–704. https://doi.org/10.5194/nhess-16-675-2016.
- Farquharson, J.I., Wadsworth, F.B., 2018. Upscaling permeability in anisotropic volcanic systems. J. Volcanol. Geotherm. Res. 364, 35–47. https://doi.org/10.1016/j. jvolgeores.2018.09.002.
- Farquharson, J.I., James, M.R., Tuffen, H., 2015. Examining rhyolite lava flow dynamics through photo-based 3D reconstructions of the 2011–2012 lava flowfield at Cordón-Caulle, Chile. J. Volcanol. Geotherm. Res. 304, 336–348. https://doi.org/10.1016/j. jvolgeores.2015.09.004.
- Farquharson, J.I., Baud, P., Heap, M.J., 2017. Inelastic compaction and permeability evolution in volcanic rock. Solid Earth 8, 561–581. https://doi.org/10.5194/se-8-561-2017.
- Forte, P., Castro, J.M., 2019. H2O-content and temperature limit the explosive potential of rhyolite magma during Plinian eruptions. Earth Planet. Sci. Lett. 506, 157–167. https://doi.org/10.1016/j.epsl.2018.10.041.
- Forte, P., Domínguez, L., Bonadonna, C., Gregg, C.E., Bran, D., Bird, D., Castro, J.M., 2018. Ash resuspension related to the 2011–2012 Cordón Caulle eruption, Chile, in a rural community of Patagonia, Argentina. J. Volcanol. Geotherm. Res. 350, 18–32. https://doi.org/10.1016/j.jvolgeores.2017.11.021.
- Gardner, J.E., Wadsworth, F.B., Llewellin, E.W., Watkins, J.M., Coumans, J.P., 2018. Experimental sintering of ash at conduit conditions and implications for the longevity of tuffisites. Bull. Volcanol. 80, 23. https://doi.org/10.1007/s00445-018-1202-8.
- Gerke, H.H., van Genuchten, M.T., 1993. A dual-porosity model for simulating the preferential movement of water and solutes in structured porous media. Water Resour. Res. 29, 305–319. https://doi.org/10.1029/92WR02339.
- Gonnermann, H.M., 2015. Magma fragmentation. Annu. Rev. Earth Planet. Sci. 43, 431–458. https://doi.org/10.1146/annurev-earth-060614-105206.
- Gonnermann, H.M., Manga, M., 2003. Explosive volcanism may not be an inevitable consequence of magma fragmentation. Nature 426, 432–435. https://doi.org/ 10.1038/nature02138.
- Gonnermann, H.M., Manga, M., 2005. Flow banding in obsidian: a record of evolving textural heterogeneity during magma deformation. Earth Planet. Sci. Lett. 236, 135–147. https://doi.org/10.1016/j.epsl.2005.04.031.
- Gonnermann, H.M., Manga, M., 2007. The fluid mechanics inside a volcano. Annu. Rev. Fluid Mech. 39, 321–356. https://doi.org/10.1146/annurev. fluid 39.050905.110207
- Gonnermann, H.M., Manga, M., Fagents, S.A., 2013. Dynamics of magma ascent in the volcanic conduit. In: Gregg, T.K.P., Lopes, R.M.C. (Eds.), Modeling Volcanic Processes: The Physics and Mathematics of Volcanism. Cambridge University Press, Cambridge. pp. 55–84. https://doi.org/10.1017/CBO9781139021562.004.
- Cambridge, pp. 55–84. https://doi.org/10.1017/CBO9781139021562.004.

 Gonnermann, Helge M., Giachetti, T., Fliedner, C., Nguyen, C.T., Houghton, B.F., Crozier, J.A., Carey, R.J., 2017. Permeability during magma expansion and compaction. J. Geophys. Res. Solid Earth 122, 9825–9848. https://doi.org/10.1002.2017JB014783.
- Heap, M.J., Xu, T., Kushnir, A.R.L., Kennedy, B.M., Chen, C., 2015. Fracture of magma containing overpressurised pores. J. Volcanol. Geotherm. Res. 301, 180–190. https://doi.org/10.1016/j.jvolgeores.2015.05.016.
- Heap, M.J., Tuffen, H., Wadsworth, F.B., Reuschlé, T., Castro, J.M., Schipper, C.I., 2019. The permeability evolution of tuffisites and implications for outgassing through dense rhyolitic magma. J. Geophys. Res. Solid Earth 124, 8281–8299. https://doi. org/10.1029/2018JB017035.
- Hess, K.U., Dingwell, D.B., 1996. Viscosities of hydrous leucogranitic melts: a non-Arrhenian model. Am. Mineral. 81, 1297–1300.
- Huppert, H.E., Woods, A.W., 2002. The role of volatiles in magma chamber dynamics. Nature 420, 493–495. https://doi.org/10.1038/nature01211.
- Jaupart, C., 1998. Gas loss from magmas through conduit walls during eruption. Geol. Soc. Lond., Spec. Publ. 145, 73–90. https://doi.org/10.1144/GSL. SP.1996.145.01.05.
- Jaupart, C., Allègre, C.J., 1991. Gas content, eruption rate and instabilities of eruption regime in silicic volcanoes. Earth Planet. Sci. Lett. 102, 413–429. https://doi.org/ 10.1016/0012-821X(91)90032-D.

- Jay, J., Costa, F., Pritchard, M., Lara, L., Singer, B., Herrin, J., 2014. Locating magma reservoirs using InSAR and petrology before and during the 2011–2012 Cordón Caulle silicic eruption. Earth Planet. Sci. Lett. 395, 254–266. https://doi.org/ 10.1016/j.epsl.2014.03.046.
- Johnson, J.B., Lyons, J.J., Andrews, B.J., Lees, J.M., 2014. Explosive dome eruptions modulated by periodic gas-driven inflation. Geophys. Res. Lett. 41, 6689–6697. https://doi.org/10.1002/2014GL061310.
- Kendrick, J.E., Lavallée, Y., Varley, N.R., Wadsworth, F.B., Lamb, O.D., Vasseur, J., 2016. Blowing off steam: tuffisite formation as a regulator for lava dome eruptions. Front. Earth Sci. 4 https://doi.org/10.3389/feart.2016.00041.
- Kolzenburg, S., Ryan, A.G., Russell, J.K., 2019. Permeability evolution during non-isothermal compaction in volcanic conduits and tuffisite veins: Implications for pressure monitoring of volcanic edifices. Earth Planet. Sci. Lett. 527, 115783 https://doi.org/10.1016/j.epsl.2019.115783.
- Kozono, T., Koyaguchi, T., 2009a. Effects of relative motion between gas and liquid on 1-dimensional steady flow in silicic volcanic conduits: 1. An analytical method. J. Volcanol. Geotherm. Res. 180, 21–36. https://doi.org/10.1016/j.jvolgeores.2008.11.006.
- Kozono, T., Koyaguchi, T., 2009b. Effects of relative motion between gas and liquid on 1-dimensional steady flow in silicic volcanic conduits: 2. Origin of diversity of eruption styles. J. Volcanol. Geotherm. Res. 180, 37–49. https://doi.org/10.1016/j.jvolgeores.2008.11.007.
- Kozono, T., Koyaguchi, T., 2012. Effects of gas escape and crystallization on the complexity of conduit flow dynamics during lava dome eruptions. J. Geophys. Res. Solid Earth 117. https://doi.org/10.1029/2012JB009343.
- La Spina, G., de Michieli Vitturi, M., Clarke, A.B., 2017. Transient numerical model of magma ascent dynamics: application to the explosive eruptions at the Soufrière Hills Volcano. J. Volcanol. Geotherm. Res. 336, 118–139. https://doi.org/10.1016/j. jvolgeores.2017.02.013.
- Lamur, A., Kendrick, J.E., Wadsworth, F.B., Lavallée, Y., 2019. Fracture healing and strength recovery in magmatic liquids. Geology 47, 195–198. https://doi.org/ 10.1130/G45512.1.
- Llewellin, E.W., Manga, M., 2005. Bubble suspension rheology and implications for conduit flow. J. Volcanol. Geotherm. Res. 143, 205–217. https://doi.org/10.1016/j. jvolgeores.2004.09.018.
- Major, J.J., Lara, L.E., 2013. Overview of Chaitén Volcano, Chile, and its 2008-2009 eruption. Andean Geol. 40. 196–215. https://doi.org/10.5027/andgeoV40n2-a01.
- Manga, M., Fauria, K.E., Lin, C., Mitchell, S.J., Jones, M., Conway, C.E., Degruyter, W., Hosseini, B., Carey, R., Cahalan, R., Houghton, B.F., White, J.D.L., Jutzeler, M., Soule, S.A., Tani, K., 2018. The pumice raft-forming 2012 Havre submarine eruption was effusive. Earth Planet. Sci. Lett. 489, 49–58. https://doi.org/10.1016/j.epsl.2018.02.025.
- Manning, C.E., Ingebritsen, S.E., 1999. Permeability of the continental crust: Implications of geothermal data and metamorphic systems. Rev. Geophys. 37, 127–150. https://doi.org/10.1029/1998RG900002.
- Marble, F.E., 1970. Dynamics of dusty gases. Annu. Rev. Fluid Mech. 2, 397–446. https://doi.org/10.1146/annurev.fl.02.010170.002145.
- Mastin, L.G., 2002. Insights into volcanic conduit flow from an open-source numerical model. Geochem. Geophys. Geosyst. 3, 1–18. https://doi.org/10.1029/ 2001GC000192.
- Melnik, O., Barmin, A.A., Sparks, R.S.J., 2005. Dynamics of magma flow inside volcanic conduits with bubble overpressure buildup and gas loss through permeable magma. J. Volcanol. Geotherm. Res. 143, 53–68. https://doi.org/10.1016/j. ivolgeores.2004.09.010.
- Michaut, C., Bercovici, D., Sparks, R.S.J., 2009. Ascent and compaction of gas rich magma and the effects of hysteretic permeability. Earth Planet. Sci. Lett. 282, 258–267. https://doi.org/10.1016/j.epsl.2009.03.026.
- Michaut, C., Ricard, Y., Bercovici, D., Sparks, R.S.J., 2013. Eruption cyclicity at silicic volcanoes potentially caused by magmatic gas waves. Nat. Geosci. 6, 856–860. https://doi.org/10.1038/ngeo1928.
- Mitchell, K.L., 2005. Coupled conduit flow and shape in explosive volcanic eruptions. J. Volcanol. Geotherm. Res. 143, 187–203. https://doi.org/10.1016/j. jvolgeores.2004.09.017.
- Munson, B., Young, D., Okiishi, T., 1994. Fundamentals of Fluid Mechanics, 2nd ed. John Wiley and Sons Ltd.
- National Academies of Sciences, 2017. Volcanic Eruptions and Their Repose, Unrest, Precursors, and Timing. National Academies Press, Washington, D.C. https://doi. org/10.17226/24650.
- Neuberg, J.W., Tuffen, H., Collier, L., Green, D., Powell, T., Dingwell, D., 2006. The trigger mechanism of low-frequency earthquakes on Montserrat. J. Volcanol. Geotherm. Res. 153, 37–50. https://doi.org/10.1016/j.jvolgeores.2005.08.008.
- Newman, S., Lowenstern, J.B., 2002. VolatileCalc: a silicate melt–H2O–CO2 solution model written in Visual basic for excel. Comput. Geosci. 28, 597–604. https://doi. org/10.1016/S0098-3004(01)00081-4.
- Ni, H., Zhang, Y., 2008. H2O diffusion models in rhyolitic melt with new high pressure data. Chem. Geol. 250, 68–78. https://doi.org/10.1016/j.chemgeo.2008.02.011.
- Noguchi, S., Toramaru, A., Nakada, S., 2008. Groundmass crystallization in dacite dykes taken in Unzen Scientific Drilling Project (USDP-4). J. Volcanol. Geotherm. Res. 175, 71–81. https://doi.org/10.1016/j.jvolgeores.2008.03.037.
- Okumura, S., Nakamura, M., Tsuchiyama, A., Nakano, T., Uesugi, K., 2008. Evolution of bubble microstructure in sheared rhyolite: Formation of a channel-like bubble network. J. Geophys. Res. Solid Earth 113. https://doi.org/10.1029/2007JB005362.
- Okumura, S., Nakamura, M., Takeuchi, S., Tsuchiyama, A., Nakano, T., Uesugi, K., 2009. Magma deformation may induce non-explosive volcanism via degassing through bubble networks. Earth Planet. Sci. Lett. 281, 267–274. https://doi.org/10.1016/j.epsl.2009.02.036.

- Okumura, S., Nakamura, M., Nakano, T., Uesugi, K., Tsuchiyama, A., 2010. Shear deformation experiments on vesicular rhyolite: Implications for brittle fracturing, degassing, and compaction of magmas in volcanic conduits. J. Geophys. Res. Solid Earth 115. https://doi.org/10.1029/2009JB006904.
- Okumura, S., Nakamura, M., Uesugi, K., Nakano, T., Fujioka, T., 2013. Coupled effect of magma degassing and rheology on silicic volcanism. Earth Planet. Sci. Lett. 362, 163–170. https://doi.org/10.1016/j.epsl.2012.11.056.
- Paisley, R., Berlo, K., Ghaleb, B., Tuffen, H., 2019a. Geochemical constraints on the role of tuffisite veins in degassing at the 2008–09 Chaitén and 2011–12 Cordón Caulle rhyolite eruptions. J. Volcanol. Geotherm. Res. 380, 80–93. https://doi.org/ 10.1016/j.jvolgeores.2019.05.013.
- Paisley, R., Berlo, K., Whattam, J., Schipper, C.I., Tuffen, H., 2019b. Degassing-induced chemical heterogeneity at the 2011-2012 Cordón Caulle eruption. Volcanica 2, 211–237. https://doi.org/10.30909/vol.02.02.211237.
- Pallister, J.S., Diefenbach, A.K., Burton, W.C., Muñoz, J., Griswold, J.P., Lara, L.E., Lowenstern, J.B., Valenzuela, C.E., 2013. The Chaitén rhyolite lava dome: Eruption sequence, lava dome volumes, rapid effusion rates and source of the rhyolite magma. Andean Geol. 40, 277–294. https://doi.org/10.5027/andgeoV40n2-a06.
- Papale, P., 1999. Strain-induced magma fragmentation in explosive eruptions. Nature 397, 425–428. https://doi.org/10.1038/17109.
- Pistolesi, M., Cioni, R., Bonadonna, C., Elissondo, M., Baumann, V., Bertagnini, A., Chiari, L., Gonzales, R., Rosi, M., Francalanci, L., 2015. Complex dynamics of smallmoderate volcanic events: the example of the 2011 rhyolitic Cordón Caulle eruption, Chile. Bull. Volcanol. 77, 3. https://doi.org/10.1007/s00445-014-0898-3.
- Polacci, M., Papale, P., Del Seppia, D., Giordano, D., Romano, C., 2004. Dynamics of magma ascent and fragmentation in trachytic versus rhyolitic eruptions. J. Volcanol. Geotherm. Res. 131, 93–108. https://doi.org/10.1016/S0377-0273(03)00319-6.
- Rust, A.C., Cashman, K.V., 2004. Permeability of vesicular silicic magma: inertial and hysteresis effects. Earth Planet. Sci. Lett. 228, 93–107. https://doi.org/10.1016/j. epsl.2004.09.025.
- Saubin, E., Tuffen, H., Gurioli, L., Owen, J., Castro, J.M., Berlo, K., McGowan, E.M., Schipper, C.I., Wehbe, K., 2016. Conduit dynamics in transitional rhyolitic activity recorded by tuffisite vein textures from the 2008–2009 Chaitén Eruption. Front. Earth Sci. 4 https://doi.org/10.3389/feart.2016.00059.
- Schipper, C.I., Castro, J.M., Tuffen, H., James, M.R., How, P., 2013. Shallow vent architecture during hybrid explosive-effusive activity at Cordón Caulle (Chile, 2011–12): evidence from direct observations and pyroclast textures. J. Volcanol. Geotherm. Res. 262, 25–37. https://doi.org/10.1016/j.ivolgeores.2013.06.005.
- Schipper, C.I., Castro, J.M., Tuffen, H., Wadsworth, F.B., Chappell, D., Pantoja, A.E., Simpson, M.P., Le Ru, E.C., 2015. Cristobalite in the 2011–2012 Cordón Caulle eruption (Chile). Bull. Volcanol. 77, 34. https://doi.org/10.1007/s00445-015-0925-
- Schipper, C.I., Castro, J., Kennedy, B., Christenson, B., Aiuppa, A., Alloway, B., Forte, P., Seropian, G., Tuffen, H., 2019. Halogen (Cl, F) release during explosive, effusive, and intrusive phases of the 2011 rhyolitic eruption at Cordón Caulle volcano (Chile). Volcanica 2, 73–90. https://doi.org/10.30909/vol.02.01.7390.
- Schipper, C.I., Castro, J.M., Kennedy, B.M., Tuffen, H., Whattam, J., Wadsworth, F.B., Paisley, R., Fitzgerald, R.H., Rhodes, E., Schaefer, L.N., Ashwell, P.A., Forte, P., Seropian, G., Alloway, B.V., 2021. Silicic conduits as supersized tuffisites: Clastogenic influences on shifting eruption styles at Cordón Caulle volcano (Chile). Bull. Volcanol. 83, 11. https://doi.org/10.1007/s00445-020-01432-1.
- Seropian, G., Schipper, C.I., Harmon, L.J., Smithies, S.L., Kennedy, B.M., Castro, J.M., Alloway, B.V., Forte, P., 2021. A century of ongoing silicic volcanism at Cordón Caulle, Chile: New constraints on the magmatic system involved in the 1921–1922, 1960 and 2011–2012 eruptions. J. Volcanol. Geotherm. Res. 420, 107406 https:// doi.org/10.1016/j.jvolgeores.2021.107406.

- Shea, T., Gurioli, L., Houghton, B.F., 2012. Transitions between fall phases and pyroclastic density currents during the AD 79 eruption at Vesuvius: building a transient conduit model from the textural and volatile record. Bull. Volcanol. 74, 2363–2381. https://doi.org/10.1007/s00445-012-0668-z.
- Slezin, Yu.B., 2003. The mechanism of volcanic eruptions (a steady state approach).
 J. Volcanol. Geotherm. Res. 122, 7–50. https://doi.org/10.1016/S0377-0273(02)
 00464.3
- Stasiuk, M.V., Barclay, J., Carroll, M.R., Jaupart, C., Ratté, J.C., Sparks, R.S.J., Tait, S.R., 1996. Degassing during magma ascent in the Mule Creek vent (USA). Bull. Volcanol. 58, 117–130. https://doi.org/10.1007/s004450050130.
- Sun, D., Roth, S., Lewis, J.P., Black, M.J., 2008. Learning optical flow. In: Forsyth, D., Torr, P., Zisserman, A. (Eds.), Lecture Notes in Computer Science, vol. 5304. Springer, pp. 83–97.
- Tuffen, H., Dingwell, D., 2005. Fault textures in volcanic conduits: evidence for seismic trigger mechanisms during silicic eruptions. Bull. Volcanol. 67, 370–387. https:// doi.org/10.1007/s00445-004-0383-5.
- Tuffen, H., Dingwell, D.B., Pinkerton, H., 2003. Repeated fracture and healing of silicic magma generate flow banding and earthquakes? Geology 31, 1089. https://doi.org/ 10.1130/G19777.1.
- Tuffen, H., Smith, R., Sammonds, P.R., 2008. Evidence for seismogenic fracture of silicic magma. Nature 453, 511–514. https://doi.org/10.1038/nature06989.
- Tuffen, H., James, M.R., Castro, J.M., Schipper, C.I., 2013. Exceptional mobility of an advancing rhyolitic obsidian flow at Cordón Caulle volcano in Chile. Nat. Commun. 4, 2709. https://doi.org/10.1038/ncomms3709.
- Unwin, H.E., Tuffen, H., Phillips, E., Wadsworth, F.B., James, M.R., 2021. Pressure-Driven opening and filling of a Volcanic Hydrofracture Recorded by Tuffisite at Húsafell, Iceland: a potential Seismic Source. Front. Earth Sci. 9 https://doi.org/ 10.3389/feart.2021.668058.
- Vasseur, J., Wadsworth, F.B., Lavallée, Y., Hess, K.-U., Dingwell, D.B., 2013. Volcanic sintering: Timescales of viscous densification and strength recovery. Geophys. Res. Lett. 40, 5658–5664. https://doi.org/10.1002/2013GL058105.
- Wadsworth, F.B., Llewellin, E.W., Vasseur, J., Gardner, J.E., Tuffen, H., 2020. Explosive-effusive volcanic eruption transitions caused by sintering. Sci. Adv. 6 https://doi.org/10.1126/sciadv.aba7940.
- Wallace, P., Plank, T., Edmonds, M., Hauri, E., 2015. Volatiles in magmas. In: Sigurdsson, Haraldur (Ed.), The Encyclopedia of Volcanoes, 2nd edition. Elsevier, pp. 163–183.
- Westrich, H.R., Stockman, H.W., Eichelberger, J.C., 1988. Degassing of rhyolitic magma during ascent and emplacement. J. Geophys. Res. Solid Earth 93, 6503. https://doi. org/10.1029/JB093iB06p06503.
- Wilson, T., Stewart, C., Bickerton, H., Baxter, P., Outes, A., Villarosa, G., Rovere, E., 2013. Impacts of the June 2011 Puyehue-Cordón Caulle volcanic complex eruption on urban infrastructure, agriculture and public health. GNS Sci. 2012/20, 1–88.
- Winslow, H., Ruprecht, P., Gonnermann, H.M., Phelps, P.R., Muñoz-Saez, C., Delgado, F., Pritchard, M., Amigo, A., 2022. Insights for crystal mush storage utilizing mafic enclaves from the 2011–12 Cordón Caulle eruption. Sci. Rep. 12, 9734. https://doi. org/10.1038/s41598-022-13305-v.
- Wong, Y.-Q., Segall, P., Bradley, A., Anderson, K., 2017. Constraining the Magmatic System at Mount St. Helens (2004-2008) using Bayesian inversion with physicsbased models including gas escape and crystallization. J. Geophys. Res. Solid Earth 122, 7789–7812. https://doi.org/10.1002/2017JB014343.
- Woods, A.W., Koyaguchi, T., 1994. Transitions between explosive and effusive eruptions of silicic magmas. Nature 370, 641–644. https://doi.org/10.1038/370641a0.
- Yoshida, S., Koyaguchi, T., 1999. A new regime of volcanic eruption due to the relative motion between liquid and gas. J. Volcanol. Geotherm. Res. 89, 303–315. https://doi.org/10.1016/S0377-0273(99)00005-0.